
















RESEARCH ARTICLE | APRIL 17 2024


Deep-reactive ion etching of silicon nanowire arrays at cryogenic temperatures ^F

Jiushuai Xu ; Andam Deatama Refino ; Alexandra Delvallée ; Sebastian Seibert ; Christian Schwalb ; Poul Erik Hansen ; Martin Foldyna ; Lauryna Siaudinyte ; Gerry Hamdana ; Hutomo Suryo Wasisto ; Jonathan Kottmeier ; Andreas Dietzel ; Thomas Weimann ; Jan Kristen Prüssing ; Hartmut Bracht ; Erwin Peiner 




Appl. Phys. Rev. 11, 021411 (2024)

<https://doi.org/10.1063/5.0166284>



Biomicrofluidics
Special Topic:
Microfluidic Biosensors

Submit Today



Deep-reactive ion etching of silicon nanowire arrays at cryogenic temperatures

Cite as: Appl. Phys. Rev. **11**, 021411 (2024); doi: [10.1063/5.0166284](https://doi.org/10.1063/5.0166284)

Submitted: 4 July 2023 · Accepted: 19 March 2024 ·

Published Online: 17 April 2024



View Online



Export Citation



CrossMark

Jiushuai Xu,^{1,2,a)}  Andam Deatama Refino,^{1,2}  Alexandra Delvallée,³  Sebastian Seibert,⁴  Christian Schwalb,⁴  Poul Erik Hansen,⁵  Martin Foldyna,⁶  Lauryna Siaudinyte,⁷  Gerry Hamdana,¹  Hutomo Suryo Wasisto,¹  Jonathan Kottmeier,⁸  Andreas Dietzel,⁸  Thomas Weimann,⁹  Jan Kristen Prüssing,¹⁰  Hartmut Bracht,¹⁰  and Erwin Peiner^{1,2} 

AFFILIATIONS

¹Institute of Semiconductor Technology, Technische Universität Braunschweig, 38106 Braunschweig, Germany

²Laboratory for Emerging Nanometrology (LENA), Technische Universität Braunschweig, 38106 Braunschweig, Germany

³Laboratoire National de métrologie et d'Essais (LNE), 78197 Trappes Cedex, France

⁴Quantum Design Microscopy GmbH, 64293 Darmstadt, Germany

⁵Danish Fundamental Metrology (DFM), DK-2970 Hørsholm, Denmark

⁶LPICM, CNRS, École Polytechnique, Institut Polytechnique de Paris, 91128 Palaiseau, France

⁷VSL National Metrology Institute, 2629JA Delft, The Netherlands

⁸Institute of Microtechnology (IMT), Technische Universität Braunschweig, 38124 Braunschweig, Germany

⁹Physikalisch-Technische Bundesanstalt (PTB), 38116 Braunschweig, Germany

¹⁰Institute of Materials Physics, University of Münster, 48149 Münster, Germany

^{a)} Author to whom correspondence should be addressed: xujiushuai@qq.com

ABSTRACT

The pursuit of sculpting materials at increasingly smaller and deeper scales remains a persistent subject in the field of micro- and nanofabrication. Anisotropic deep-reactive ion etching of silicon at cryogenic temperatures (cryo-DRIE) was investigated for fabricating arrays of vertically aligned Si nanowires (NWs) of a large range of dimensions from micrometers down to 30 nm in diameter, combined with commonly used wafer-scale lithography techniques based on optical, electron-beam, nanoimprint, and nanosphere/colloidal masking. Large selectivity of ~ 100 to 120 and almost 700 was found with resists and chromium hard masks, respectively. This remarkable selectivity enables the successful transfer of patterned geometries while preserving spatial resolution to a significant extent. Depending on the requirements by applications, various shapes, profiles, and aspect ratios were achieved by varying process parameters synchronously or asynchronously. High aspect ratios of up to 100 comparable to the best result by metal-assisted wet-chemical etching and sub- μm trenches by DRIE were obtained with NW diameter of 200 nm, at an etch rate of $\sim 4 \mu\text{m}/\text{min}$ without being collapsed. At the same time, low surface roughness values were maintained on the NW top, sidewall, and bottom surface of ~ 0.3 , ~ 13 , and ~ 2 nm, respectively, as well as high pattern fidelity and integrity, which were measured using angle-resolved Fourier microscopy, combined atomic force, and scanning electron microscopy on selected NWs. This work establishes the foundation in the controllable development of Si nanoarchitectures, especially at sub-100 nm structures, for energy-harvesting and storage, damage-free optoelectronics, quantum, photovoltaics, and biomedical devices.

© 2024 Author(s). All article content, except where otherwise noted, is licensed under a Creative Commons Attribution (CC BY) license (<https://creativecommons.org/licenses/by/4.0/>). <https://doi.org/10.1063/5.0166284>

I. INTRODUCTION

In the last two decades, fabrication of high-aspect-ratio nanostructures has attracted great attention attributing to its spreading applications in various fields. Large-scale ordered arrays of vertically aligned Si nanowires (VA-Si-NWs) of defined surface roughness represent a new

class of three-dimensional structures, exhibiting unique and superior optical, electric, mechanical, thermal, and chemical properties,¹ due to their unique features, including high surface-to-volume ratio, high electron mobility, anti-reflection, chemical-/bio compatibility, and elasticity. They have shown great promise and are actively studied for various

applications, such as the next generation of energy harvesters (e.g., photovoltaics and thermoelectrics) and storage (e.g., lithium-ion batteries (LIBs) and supercapacitors²), optical devices (sub-100-nm resolution metasurfaces³), field-effect transistors,⁴ and chemical and biological sensors.⁵

The Si-NW-produced Seebeck voltages are an order of magnitude higher than bulk Si when stacked with it.⁶ Thermal conductivity of Si-NWs can be further reduced by increasing their length, surface roughness, or doping concentration, and decreasing their diameters.⁷ For the Si-NWs used in photovoltaics (PV), the light-harvesting ability of Si-NWs increases linearly with their lengths,⁸ while asymmetric pencil-shaped arrays of Si-NWs keep the light-reflectance below 10%,⁹ which is favorable for enhancing conversion efficiency. Moreover, black silicon, distinguished by its disordered structure encompassing elevated features such as spikes, needles, and pyramids, as well as deeper elements like pores, holes, and craters, demonstrates favorable light absorption characteristics.^{10,11} It effectively captures sunlight, particularly within the near-mid-infrared wavelength range. Additionally, a substantial increase in absorption on the surface-microstructured silicon through femtosecond laser irradiation in ambient air with sulfur hexafluoride (SF₆) gas has been observed across a broad wavelength range, extending from 0.3 to 16 μm .¹² The extension of this spectral range, reaching wavelengths up to 25 μm , can be achieved through the synergistic effects of morphology (high-aspect-ratio conical nanostructures) and volume doping.¹³ For enhanced charge storage in LIBs, anodes composed of well-ordered NW arrays are favored over randomly arranged or disordered configurations.¹⁴ Correspondingly, photocathodes made of highly ordered Si-NW arrays (Si-NWAs), with optimized structural parameters such as length, diameter, and pitch, exhibit superior photoelectrochemical (PEC) performance, characterized by elevated saturated photocurrent densities and a lowered onset potential for the hydrogen evolution reaction (HER).¹⁵ The light-trapping ability of conventional nanostructured black silicon in PV devices toward improved broadband absorption is achieved using black silicon of combined ordered micropores and disordered nanopores.¹⁶ These ordered pores offer sufficient space for incorporating functional materials while promoting an increased optical path length, facilitated by the low roughness of the sidewalls. Additionally, the unordered nanopores positioned at the top and at the base of the nanostructure facilitate coupling between incident solar radiation and the silicon substrate. In addition, highly doped high area-density Si-NWs improve the device performance further.¹⁷ In the water splitting process, Si-NWs act in PEC cathodes, where less coalesced, highly dense and lengthier *p*-type Si-NWs have proven to be better for natural water reduction.¹⁸ In addition, various diameters and inter-spaces are required for bio and gas sensing applications.⁵ In summary, target values for NW diameter, height, and area density are in the ranges of ten to hundred nanometers, tens of micrometers (or higher), and $>10^8 \text{ cm}^{-2}$, respectively. For both phenomenological studies and the accomplishment of practical applications of Si-NWs, fabrication of Si-NWs with precise control of density, dimensions, and crystallographic orientation will be of great value. Therefore, a universal technique offering flexibility for the fabrication of various Si-NWs is required.

Depending on the employed fabrication methodologies, realization of Si-NWs is generally categorized into bottom-up and top-down techniques, by adding or removing correspondingly Si material. The bottom-up approach by NW-growth using a metal catalyst has enabled

the routine fabrication of sophisticated 1D devices that is otherwise not possible with conventional top-down approaches. This growth method is most frequently described through the vapor-liquid-solid (VLS) mechanism.¹⁹ Due to the concerns of diffusion of the catalyst, which is related to the necessity of high temperatures during Si epitaxial processes, forming deep traps in the NWs, electronic and optical devices suffer from reduced minority carrier lifetime.^{20,21} A further difficulty is the lack of orientation control, i.e., obtaining Si-NWs in the $\langle 100 \rangle$ -axis orientation is often difficult, integration of VLS NWs into complementary metal-oxide-semiconductor (CMOS) technology is limited.^{22,23} Anodic aluminum oxide (AAO), which offers ordered honeycomb arrays of nanopores, can serve as a template to grow epitaxial Si(100) NWs on a Si(100) substrate.²⁴ Electroless deposited gold within the HF-etched pores in the AAO film functions as the catalyst for VLS Si-growth. In addition, complementary metal-oxide-semiconductor (CMOS)-compatible heteroepitaxial growth of III/V semiconductor NWs can be achieved through lithographically patterned holes in a silicon nitride template.²⁵ Alternatively, etched ion-track membranes, glass, mica sheets, or zeolites can be used as substitutes for AAO in catalyst-free electrochemical growth of metal, semiconductor, or metal oxide NWs.²⁶ Template-assisted electrochemical growth of metal (Cu, Au, Ag, Ni, Pt) NWs for applications such as pressure sensors²⁷ or low-temperature die attach, achieved by pressing two surfaces with NWs together at room temperature,²⁸ have been reported. The presence of copper oxide, influencing the elastic modulus of copper nanowires, can be mitigated through treatment with forming gas plasma or exposure to formic acid vapor.²⁸

Currently, the most common way for fabricating ordered vertically aligned Si-NWAs of high area density is the top-down method, either using wet or dry etching methods.^{29,30} Top-down fabrication of Si-NWs can generally be realized by area-selective removal of Si materials, using either plasma-based dry etching [i.e., the Bosch or pseudo-Bosch process, and cryogenic deep-reactive ion etching (cryo-DRIE)] or wet/gas-chemical etching [e.g., metal-assisted chemical etching (MacEtch or MACE), etc.]. Using wet-MacEtch combined with nanosphere lithography [NSL, also known as colloidal lithography (CL)]³¹ or nanoimprint lithography (NIL), corresponding large-scale ordered Si-NWAs can be realized with low cost or high structure fidelity and purity, respectively.³² Nevertheless, regions of Si-NWAs having large aspect ratio may collapse and suffer from structural failure. Here, the liquid etchant is responsible for forces (van der Waals force, capillary force) generating an agglomeration of adjacent NWs into bunches.³³ Bunches of crystalline sub-5 nm Si-NWs of an extreme aspect ratio of >10000 can be realized in a chemical vapor etching (CVE) process using silicon tetrachloride (SiCl₄), which however requires temperatures of 1000 °C–1150 °C.³⁴ Recently, a new method of gas-MacEtch has been reported, wherein hydrofluoric acid (HF) is evaporated from liquid solution and heated typically at temperatures higher than 40 °C.³⁵ Liquid condensation on Si-NWs during the MacEtch process is therefore prevented, realizing minimized stiction or deflection of Si-NWs due to liquid drying with respect to the conventional wet-MacEtch process. However, non-uniform height and bottom surface are often observed on large scales. Dry etching is one of the preferred pattern transfer methods because it allows extensive parameter tunability, permitting optimization of the etched profile of high-aspect-ratio nanostructures, e.g., sub- μm trenches in silicon.³⁶ Unlike wet-chemical etching, dry etching has the advantage of liquid-free

processing, which mitigates issues such as stiction, and can be more readily incorporated into fully automated processes.³⁷ In addition, since dry etching has the capability of transferring patterned geometries without significantly losing spatial resolution, it offers a considerable competitive advantage in microelectronics industry.³⁸ However, the noble-metal catalyst, which is conventionally used in MacEtch, causes deep-level defects in silicon and is thus not applied in both front-end and back-end lines of the CMOS fabrication process.³⁹ Other CMOS-compatible catalysts like titanium nitride (TiN), graphene, and tungsten (W), etc., show much larger activity and excessive hole-generation in the MacEtch process, which may lead to porous NWs even at low aspect ratios.⁴⁰ Instead, due to its reliability and versatility, the inductively coupled plasma (ICP) reactor has been widely used nowadays for mass production and low-cost anisotropic Si etching.

High aspect ratio and anisotropic etching are commonly achieved by the ICP-based Bosch process, which is a repetition of two etching steps: first, a standard nearly isotropic etching is carried out using sulfur hexafluoride (SF₆) gas and, second, deposition of a passivation layer is performed by octafluorocyclobutane (C₄F₈) gas. The lateral etching component limits the maximum achievable aspect ratio for recessed nanostructures and leads to the well-known scalloping effect on the etched sidewalls.^{41,42} Alternatively, a non-switching pseudo-Bosch recipe has been developed, where etching and passivation gases are introduced to the reaction chamber at the same time, resulting in a continuous sidewalls passivation instead of cyclical passivation. The pseudo-Bosch recipe can eliminate the scalloping effect and realize controllable etching profiles by tuning the gas ratio, while resulting in lower etching rate and selectivity to mask materials, compared to the standard Bosch process.⁴¹ To push the technological limits of fabricating VA-Si-NWAs further to smaller diameters and higher aspect ratios, many attempts have been made using the Bosch and pseudo-Bosch processes, including control in ion transport,⁴³ addition of light ions with low energy to decrease the charging effect,⁴⁴ addition of hydrogen (H₂) during the passivation step,⁴⁵ introduction of a periodic O₂ plasma cleaning step,⁴¹ and adjustment of process parameters during etching and passivation.³⁸

There has magnificent work been done using DRIE at room temperature achieving Si-nanostructures of large aspect ratio⁴⁶ and small diameter⁴⁷ reaching down to 10 nm and below for individual nano-sheets.⁴⁸ In the latter case, high-quality hydrogen silsesquioxane (HSQ) resist masks with sub-10 nm resolution and aspect ratios up to 25:1 have been reproducibly generated, which were directly exposed with electron-beam lithography (EBL). Nanotrenches of 250 nm with exceedingly high aspect ratios up to 160:1 have been achieved using the Bosch process with an aluminum layer of 500 nm thickness as mask.³⁶ All the aforementioned studies are noteworthy; however, etching Si fins and trenches vs Si-NWAs presents distinct challenges owing to the well-known loading effect. The loading effect manifests as an etching rate contingent upon the surface area of the substrate exposed to chemical etching. Specifically, larger areas of substrate surface undergoing etching experience a decreased etch rate compared to smaller areas. This effect operates at both microscale levels (such as individual features or dies) and macroscale levels (across the substrate), arising from the depletion of reactants at the etched features.⁴⁹ Mitigating loading effects involves adjusting the etch rate or augmenting the available reactants for etching. Etch loading can significantly

impact etch uniformity. Studies reveal that as the percentage of exposed substrate surface increases from approximately 8% to nearly 100%, the etch rate diminishes by over 50%, and non-uniformity escalates from 2% to 35%.⁵⁰ Surface roughness of trench sidewalls in typical Bosch processes often exceeds 200 nm; however, for smaller trenches (below 5 μm), this roughness markedly decreases to levels below 25 nm.³⁶ Consequently, while etching sub-micron trenches or individual wires are relatively manageable, scaling up to large-scale or wafer-scale Si-NWAs etching poses greater difficulty and challenge.

A versatile method for fabricating ordered Si-NWAs on large scale is DRIE at cryogenic temperatures (cryo-DRIE), which can realize high-aspect-ratio Si-NWAs of a large range of dimensions without NW collapse and scalloped sidewalls. Similar to the pseudo-Bosch process, cryo-DRIE is a non-switching, anisotropic etching process in an inductive-coupled plasma (ICP) reactor, by systematic optimization of etching temperature, power of ICP and radio frequency (RF) for bias, gas-flow rates and concentrations of SF₆ and O₂, pressure in the reactor, etc. (see Fig. 1). Detailed guidelines for optimizing cryo-DRIE of Si microstructures have been given by de Boer *et al.*⁵¹ However, to obtain high-quality manufacturing and push the etching limits of Si wires further to yield ultra-high-aspect-ratio NWs, further investigation of mask fabrication and etching mechanism must be accomplished, wherein all process parameters have to be optimized. Furthermore, the etching results of nanostructures are influenced not only by process parameters but also other factors such as size, pitch, and shape of mask opening;⁵² aspect ratio of the etched features; loaded patterns;⁵³ and mask materials.⁵⁴ In this respect, our motivation is to develop a guideline for manufacturing high-quality Si-NWAs, inspecting the general availability for etching Si material of different crystal orientations and doping concentrations using various mask materials (resist and metal). We adopted ultraviolet (UV) photolithography (PL), nanosphere lithography (NSL),⁵⁵ soft UV nanoimprint lithography (NIL),⁵⁶ and electron-beam lithography (EBL) to prepare masks of different dimensions and layout designs, followed by cryo-DRIE to etch Si-NWAs of various dimensions and profiles. The comprehensive results of μm to sub-μm, especially sub-100-nm Si-NWAs, presented in this work can be useful for a wide range of applications, allowing for massive production using cryo-DRIE based on inexpensive, versatile, reproducible, and industrially compatible process possibilities.

Figure 2 illustrates the physicochemical mechanisms of anisotropic Si etching using cryo-DRIE. The basic idea of fabricating Si-NWAs using cryo-DRIE is to find a balance between surface passivation of the developing NW-sidewalls and etching of the bottom surface in between the NWs, wherein SF₆ and O₂ are used as etchant and passivation species, respectively. In the cryo-DRIE process, fluorine radicals (F^{*}) produced by the decomposition of SF₆ in an ICP source, diffuse to the Si wafer surface, where they react spontaneously with Si atoms to form volatile SiF₄, resulting in isotropic etching. At the same time, a passivation layer of SiO_xF_y is formed, which is generated by the reaction of oxygen radicals (O^{*}) with F^{*} and Si, slowing down further etching of Si until it stops.^{51,57} Especially at cryogenic temperatures, the deposition of SiO_xF_y is enhanced by reducing its chemical/radical reactivity, which has been indicated by a measured lower volatility of the silicon etching products (SiF₄).⁵¹ Accordingly, Dussart *et al.*⁵⁸ found by *in situ* experimental characterization of cryo-DRIE that SiF₄ can participate in forming the passivation layer and reinforce it.

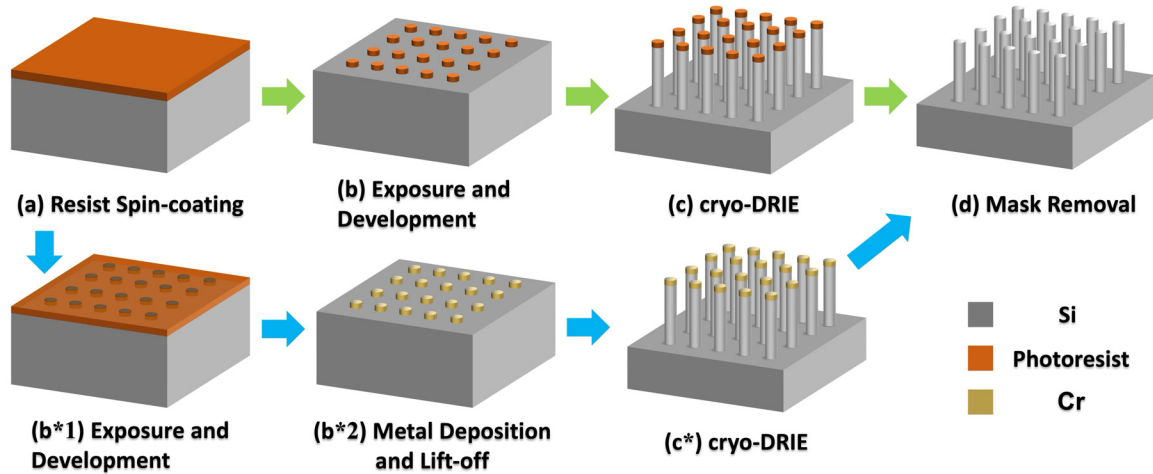


FIG. 1. Schematic processes of fabricating Si-NW arrays (Si-NWAs) using resist (a)–(c) or hard masks (a*)–(c*) prepared by nanolithography (UV-photolithography (UV-PL), UV-NIL, EBL) and liftoff followed by (c) and (c*) cryo-DRIE. Detailed descriptions of fabrication processes are available in Sec. IV. In the following, samples are classified by their designed values of diameter (D), pitch (P), and height (H) of the respective VA-Si-NWA according to D(iameter)@(itch)@(number, in nm)-H(eight) (@number, in nm), e.g., D50-P500-H200 denotes a VA-Si-NWA of 50 nm diameter, 500 nm pitch, and 200 nm height.

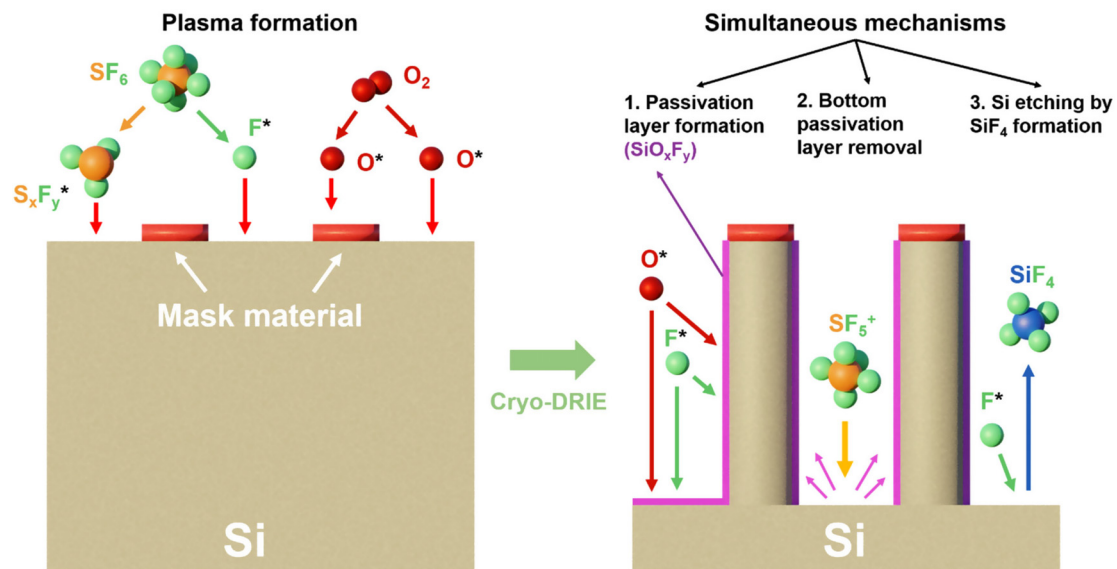


FIG. 2. Schematic of the physicochemical mechanisms of ideal anisotropic Si etching using cryo-DRIE. $S_xF_y^+$, F^* , and O^* formed in the generated plasma are diffused to the Si surface. The passivation-layer (SiO_xF_y) formation, the removal of bottom passivation layer, and Si etching by F^* occur simultaneously under cryogenic temperature. The anisotropic behavior of the process enables the mask materials to define the Si-NWA structures.

Simultaneously, ions like SF_5^+ , also generated by the decomposition of SF_6 in the ICP source, can remove the SiO_xF_y passivation layer physically even at relatively low kinetic energies as they strike the surface. This enables further chemical etching of Si in the unprotected bottom-surface areas, which are much more exposed to the directional ion bombardment than the NW-sidewall surfaces. Therefore, the sidewall surfaces will stay covered by the passivation layer blocking chemical etching, while the passivation layer formed on the bottom surface is removed, and chemical etching can be proceeded. To establish an ideal

anisotropic etching, the processes of passivation-layer formation, its removal from the bottom surfaces, and the simultaneously etching of un-passivated Si surfaces, must be maintained in delicate balance.

Several universal recipes for etching Si-NWAs, developed through systematic variations in cryo-DRIE process parameters, are presented in Table I. The selection of lithography techniques and mask materials, coupled with the desired Si-NWs features, such as height, diameter, length, pitch, and roughness, have guided the optimization of specific cryo-DRIE parameters, detailed in Sec. II C. Herein,

TABLE I. Process parameters of cryo-DRIE recipes using different masks optimized for etching Si-NW arrays (Si-NWAs) with specific features. PL: photolithography; EBL: electron-beam lithography; NIL: nanoimprint lithography, HAR: high aspect ratio, MWAs: microwire arrays.

Recipe	Features preference	T (°C)	p (Pa)	SF ₆ (sccm)	O ₂ (sccm)	ICP (W)	RF (W)
#Nano-Uniformity	High uniformity/fidelity	−95	1	60	6	150	10
#sub-100 nm-1	Low roughness, low mask undercut	−95	1	120	15	140	8
#sub-100 nm-2	Low roughness, low mask undercut	−95	1	120	14	150	8
#PL-HAR	HAR MWAs, high etch rate	−95	0.8	119	12	500	6
#NIL-HAR	HAR NWAs	−95	1	120	12	500	5
#EBL-HAR	HAR NWAs	−95	0.75	115	15	500	6

particular parameters have been deliberately chosen to attain desired characteristics in Si-NWAs. For instance, the use of high inductively coupled plasma (ICP) power is targeted for achieving elevated etch rates, while a higher O₂ ratio is favored for high-aspect-ratio (HAR) Si-NWAs. Profile adjustments of different mask layouts aligned with variations in diameters and pitches have been achieved by manipulating radio frequency (RF) power, gas ratios, and pressure settings. Section II C delves into the discussion and analysis of variations in process parameters to showcase their influence on Si etching.

Metrology of the complex 3D geometry VA-Si-NWs requires traceable-to-the-SI nanodimensional characterization including 3D form (cylindrical, prismatic, and pyramidal) and sidewall roughness. In a hybrid metrology approach, high-throughput optical measuring methods based on imaging scatterometry, which work by capturing a series of images of an illuminated sample at several wavelengths and combined with advanced atomic force microscopy (AFM) and scanning electron microscopy (SEM). Thus, the geometrical form and size of the nanostructures was imaged locally (AFM and SEM) as well as on wafer scale [i.e., scatterometry and Mueller matrix ellipsometry (MME)]. Achieving ideal fabrication is integral to establishing and optimizing the simulation and quantification of characterization systems. Conversely, an optimized characterization system facilitates a deeper comprehension of reactions and propels fabrication methods toward the optimal limit.

II. RESULTS AND DISCUSSION

A. Lithography methods/mask materials—undercut and selectivity

Novel applications, like silicon-based Li ion batteries, require HAR VA-Si-NWAs as anodes of large surface area for efficient charge cycling and the ability for accommodating stress during lithiation.² For etching such HAR VA-Si-NWAs, mask erosion (selectivity of Si vs mask) and lateral etching under the masks (undercut) are the main challenges to be overcome, since mask erosion determines the vertical aspect ratio of NWs and the lateral etching under the mask may result in a dimensional deviation from the expected vertical-sidewall-NW shape or even a falling-off of the masks from the not yet completely etched NWs. Lateral etching right under the mask is fundamentally induced by a low sticking efficiency of free radicals (F^{*}) on the Si surface, i.e., most fluorine radicals will be bounced back from the bottom surface to attack the Si on the NWs sidewalls. The Si below the masks is mainly affected, especially just after the etching has started, when the passivation layer has not sufficiently formed, leading to strong initial lateral under-mask etching.

During the process, lateral etching occurs, diminishing the precision of pattern transfer and imposing constraints on the maximum attainable height of the NW. For estimating this value, we compare for the different cryo-DRIE recipes the final diameter D_{NW} of NWs after etching to that of the initially fabricated resist nanopattern and determine a pattern-dimension-transfer-related “undercut” as the deviation of D_{NW} from the initial diameter D_{m0} of the mask disk (DIM),

$$DIM = \frac{D_{m0} - D_{NW}}{D_{m0}} \times 100\%. \quad (1)$$

The maximum height H_{max} of a NW, which can be obtained using an optimized recipe, is attained with the falling-off of the mask.

1. PL—micropillars

For micropillar arrays, photoresist patterns of nominally 1 μm in diameter, 4 μm in pitch, and ~ 200 nm in thickness (Fig. S1) have been fabricated by photolithography (PL) for etching Si-NWAs (Sec. IV A) using the process parameters of recipe #PL-HAR (Table I). The obtained Si-NWAs of ~ 1060 nm in diameter at the NW top, ~ 1220 nm in diameter at the NW bottom part, and 17.2 ± 0.1 μm in height (sidewall angle: 90.27°). If we adhere to the conventional concept of undercut, the samples do not exhibit a distinct undercut of the Si-NWs under the resist. However, in comparison with the diameter (approximately 1.2 μm) of the originally patterned resist-disks-mask, the resulting lateral dimensions of the Si-NWs have reduced to an average of ~ 1060 nm. This reduction is attributed to the progressive etching of the resist polymer. Isotropic etching not only erodes the mask disk vertically but also laterally, resulting in a decrease in the diameter of the mask disks and, consequently, Si-NWs narrower than the original disk diameters. As a result, the diameter of the fabricated Si-NWs is observed to decrease with etching time. However, due to lateral etching of the resist mask itself, an undercut between the resist mask and Si-NW is not discernible by SEM. Nevertheless, there is a diameter deviation of the obtained NWs from the initial resist nanodisks. Hence, we posit that the DIM provides a more precise definition of the mask-transfer process, using Eq. (1), and the above values we find $DIM = 13.1\%$ for the etching recipe #PL-HAR.

2. NSL—self-organized nanopatterning

Smaller lateral dimensions than with PL can be realized using nanosphere lithography (NSL) [or colloidal lithography (CL)] (Sec. IV A, process see Fig. S2), where the diameter of the masking polystyrene nanoparticles (PS-NPs) can be controllably reduced by O₂ plasma,

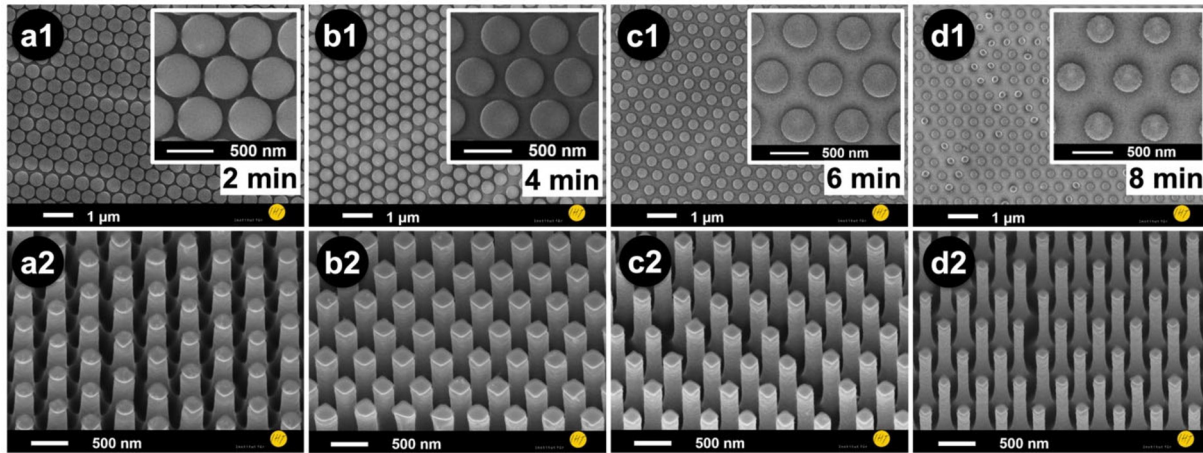


FIG. 3. Fabrication of ordered VA-Si-NWAs with different diameters using nanosphere lithography (NSL) and cryo-DRIE. (a1)–(d1), SEM top view of polystyrene nanoparticles (PS-NPs, diameter = ~ 500 nm) with defined reduction of PS-NPs dimensions using O_2 plasma, (a1) 2 min, (b1) 4 min, (c1) 6 min, and (d1) 8 min; insets are their corresponding magnified top-views. The scale bars are $1 \mu\text{m}$ and 500 nm, respectively. (a2)–(d2), 30° tilted SEM view of cryo-DRIE (recipe #sub-100 nm $^{-1}$, 20 min) fabricated Si-NWAs using corresponding PS-NPs masks (a1)–(d1), NW diameter $D_{\text{NW}} = 257$ nm (a2), 225 nm (b2), 217 nm (c2), and 146 nm (d2), aspect ratios = 7 (a2), 7 (b2), 6 (c2), and 10 (d2), NW area density = $\sim 10^7$ NWs/cm 2 . The scale bars are 500 nm.

as shown in Figs. 3(a1)–3(d1) and S2. This enables the advantage of subsequently adjustable mask diameters for etching Si-NWs of corresponding diameters. In addition, the PS-NP diameters are further reduced during cryo-DRIE as in the case of resist masks, leading to a diameter shrinkage, similar to Si-NWs obtained with PL as aforementioned (Table SI). In an ideal NSL process, wherein a uniform single PS-NP layer has formed, the pitch of the Si-NWA will be nearly equal to the diameter of the PS-NPs [Fig. 3(a1), inset]. PS-NPs of ~ 500 and ~ 200 nm in diameters have been investigated in our work, and their diameters after O_2 plasma etching of different times and diameters of Si-NWs (recipe #sub-100 nm $^{-1}$, 20 min, Table I) fabricated using cryo-DRIE through masks of these nanoparticles are shown in Table SI. The pitches between the PS-NPs and thus the areal density of the Si-NWA remains unchanged. Due to the nature of these nanoparticles, which are spin-coated onto the Si substrate in a spherical shape, the contact area between the sphere and the Si surface is significantly smaller than the diameter of the sphere itself. As a result, the Si surfaces surrounding the contact area, as well as the areas underneath the PS-NPs, exhibit weak sticking or may not adhere to the surface at all. These regions are not protected by either a masking sphere or a passivation layer. Consequently, during the etching process, free fluorine radicals may rebound and cause a more pronounced lateral etching effect compared to the use of PL masks. This is attributed to the increased exposure of the Si surface to the etching gases in the unprotected regions. On the contrary, PS-NPs under longer-time O_2 plasma etching are supposed to have smaller diameters but larger contact areas, which have been promoted by the heating generated during O_2 plasma treatment. In general, PS-NPs give thus more serious undercut than PL masks from $\text{DIM} = 31\%–44\%$ (Table SI) using recipe #sub-100 nm $^{-1}$. Furthermore, on larger areas, the 2D arrangement of the PS-NPs and, accordingly, the Si-NWA may be distorted by defects. Moreover, prolonged etching periods result in the detachment of nanoparticles from the top of formed Si-NWs, as depicted in Figs. S3, leading to the cessation of uniform etching (Fig. S4, left). Prior to cryo-DRIE, subjecting samples coated with nanoparticles to an additional annealing

process at 105°C for 2 min enhances adhesion between the nanoparticles and the sample surface. Consequently, the subsequently etched Si-NWAs exhibit reduced undercut, allowing the nanoparticles to remain atop the NWs even during extended etching durations. However, the annealing process introduces new challenges; the removal of the nanoparticles post-etching becomes arduous (Fig. S4, right).

3. NIL–high-density, large-scale nanopatterning

Nanoimprint lithography [NIL (Sec. IV A)] resist is supposed to have better sticking efficiency than PL resist, since the spin-coated film of resist is additionally pressed during UV illumination by a stamper, which can lead to less undercut during the subsequent etching. Dey *et al.* performed an experimental investigation of metals and their oxides as mask materials for Si etching using a non-switching pseudo-Bosch process.⁵⁹ For reasons that are still not well known, metal masks have been observed to show the tendency of giving more lateral undercut etching than resist, silicon oxide, or silicon nitride masks. In the present work, NIL-patterned imprint resist [UV Cur06, Fig. 4(a1)] and Cr [negative NIL-mask, followed by a liftoff process, Fig. 4(b1)] of the same layout (D800-P2400H ~ 300) have been used as a mask for etching Si-NWAs by recipe #Nano-Uniformity [30 min, Table I, Figs. 4(a2) and 4(b2)] and #NIL-HAR [10 min, Table I, Figs. 4(a3) and 4(b3)], respectively. The resulting diameters of resist and Cr masks are determined by ImageJ⁶⁰ to be $\sim 910 \pm 10$ nm and $\sim 760 \pm 10$ nm with thicknesses of $\sim 280–300$ nm. After having been processed with recipe #Nano-Uniformity (Table I), Si-NWAs of $\sim 3 \mu\text{m}$ in height have been realized using both masks. For the NWs obtained by the resist mask, an undercut has not been observed, i.e., the top diameter of the NWs has the same value as the resist nanodiscs, which is 900 ± 10 nm. On the contrary, notable etching of the Si-NWs under the Cr masks can be seen, resulting in a rough surface of the NW top parts. When we compare the Si-NWAs of Figs. 4(a3) and 4(b3), which both are $\sim 24 \mu\text{m}$ in height, i.e., an influence of mask materials on vertical etch rate is not found, the differences of their undercuts are obvious, the

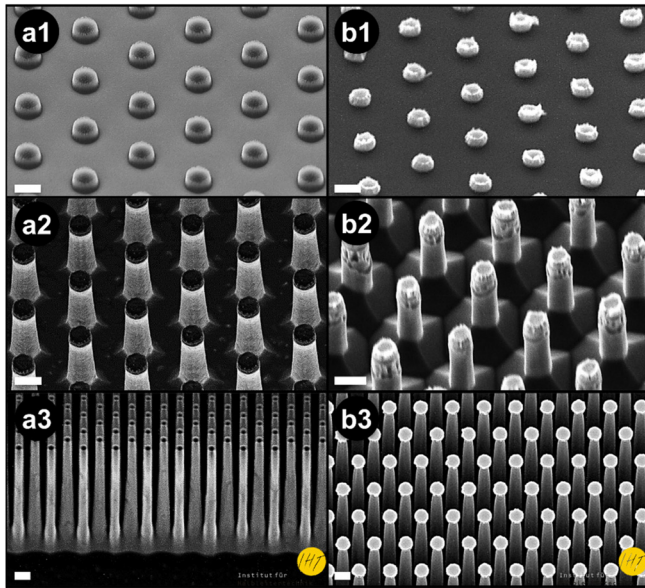


FIG. 4. SEM graphs of a UV Cur 06 resist mask [(a1), 30° tilted view] and a Cr mask [(b1), 45° tilted view], and corresponding Si-NWAs etched from them respectively [(a2) and (a3) from resist masks, (b2) and (b3) from Cr masks, 30° tilted view], by cryo-DRIE. Recipe #Nano-Uniformity of 30 min (Table I) was used for (a2) and (b2), #NIL-HAR of 10 min (Table I) for (a3) and (b3). All scale bars are 1 μm .

top-diameters of Si-NWs obtained by NIL-resists are $\sim 780 \pm 30$ nm, whereas those under Cr masks are $\sim 500 \pm 30$ nm. We correspondingly find $DIM = (14 \pm 4) \%$ and $(34 \pm 4) \%$ with UV Cur06 and Cr, respectively. Among the plausible explanations for the observed tendency of Cr for giving more lateral undercut etching than resist, a mechanism termed as metal-assisted plasma etching (MapEtch),³⁷ similar to MacEtch using a mixture of hydrofluoric acid (HF) and hydrogen peroxide (H_2O_2), have been highlighted to explain this phenomenon. In MapEtch, noble metals, such as Au and Ag lead to the formation of fluoride in the plasma and draw electrons from the Si underneath the metal (or inject holes as in MacEtch) to boost the etching there. Dey *et al.* reported that a base metal like Cr may at least slightly enhance etching of silicon underneath the mask.⁵⁹ Effects of mask material conductivity on lateral undercut etching in Si-NWs fabrication using the pseudo-Bosch process have been investigated, for etching Si-NWs of D200P500H5000 by masks of Cr (thickness: 35 nm) and Cr_2O_3 (thickness: 35 nm). There, undercuts of 34 and 18 nm have been, respectively, observed, corresponding to DIM values of 34% and 18%, respectively.⁵⁹

4. EBL–sub-30 nm nanopatterning toward high-resolution Si-NWAs

EBL has been employed to fabricate either high-resolution resist-mask nanopatterns [HSQ, poly(methyl methacrylate) (PMMA), etc.] or hard mask nanopatterns (SiO_2 , Cr, Cr_2O_3 , Al, etc.) with an additional mask material deposition and subsequent liftoff process. HSQ resist layer of 250 nm in thickness defines sub-10 nm nanolines/nanostrips and acts as dry-etch mask to transfer strips into the Si substrate to realize high-aspect-ratio sub-10 nm Si-nanofins.⁴⁸ In our

work, taking advantage of the high resolution and layout-design flexibility of EBL, Cr nanodiscs masks of diameters from 30 to 1500 nm, pitches from 500 to 5000 nm, and a thickness 30 nm have been fabricated (Fig. S5, Table. SII) and used for etching Si-NWAs by recipe #sub-100 nm-2 for 8 min (Table I), realizing corresponding Si-NWAs shown in Fig. S6 and Figs. 6(c)–6(f). To the best of our knowledge, highly ordered Si-NWAs with diameters as small as 30 nm (Fig. S6) are reported for the first time. With a proper layout-design, Si-NWAs of different diameters and pitches were etched simultaneously, and the details are shown in the following process-parameter discussion.

In addition, to compare the undercut of a different etching technique, in our work, Si-NWAs of identical dimensions have been fabricated by cryo-DRIE (recipe #sub-100 nm-2, 20 min, Table I) using Cr masks (30-nm-thick), where the undercut has been inspected to be ~ 7 nm [Fig. 5(b)], with a calculated value of $DIM \approx 7\%$. The improved etching with less undercut using cryo-DRIE may be assigned to the low reactivity of the radicals at cryogenic temperatures; therefore, Si under mask has been less etched at the initial process state when the passivation has not been formed yet. In addition, the larger Si etching undercut of the Cr mask of 300 nm thickness [Fig. 5(b2)] vs 30 nm thickness [Fig. 5(b)] can be attributed to its larger thermal compression during cooling down. The DIM values of the considered mask materials (AZ5214 resist, UV Cur 06 resist, PS-NPs, and Cr) are summarized in Table II. Masks of PS-NS show very large DIM values due to their low sticking efficiency to the substrate surface, and both PL resist (AZ5214E) and UV nanoimprint resist (UVCur06) have lower DIM values than Cr masks.

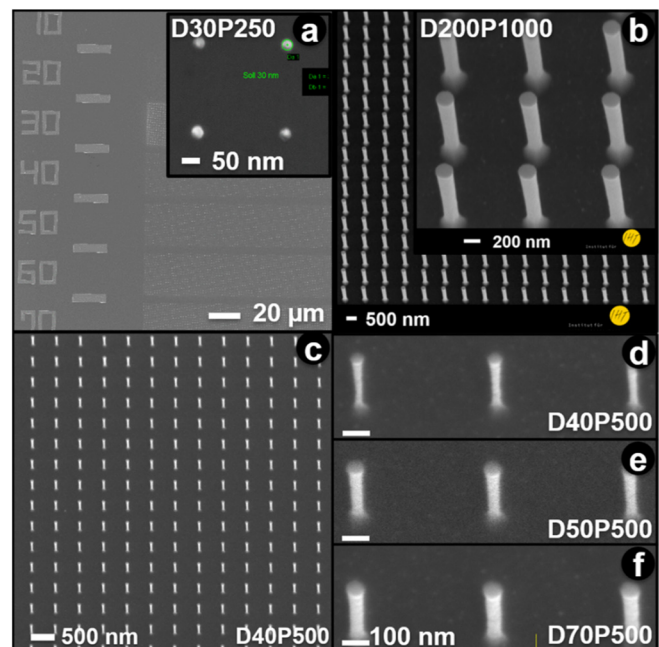


FIG. 5. SEM graphs of (a) Cr nanodisc masks with diameters from 30 nm to 70 nm, inset is the magnified view of Cr masks D30-P500-H30 (top view), (b) Si-NWAs of D200-P1000-H \sim 1260, fabricated by cryo-DRIE (recipe #sub-100 nm-2, 20 min, Table I), 30° tilted, inset is its magnified view, (c) Si-NWAs of D40-P500-H \sim 460, (d) magnified views of D40-P500-H \sim 460, (e) D50-P500-H \sim 460, and (f) D70-P500-H \sim 460 cryo-DRIE (recipe #sub-100 nm-2, 8 min, Table I).

TABLE II. Si-NWs fabricated using different masks, the deviation of NW from initial mask diameter (*DIM*), and selectivity of silicon vs mask etching using the Bosch, pseudo-Bosch, and cryo-DRIE processes (recipes see Table I).

Process	Recipe	Mask			DIM (%)	Selectivity (Si vs mask)	NW height (μm)
		Material	Thickness (nm)	Diameter (nm)			
Bosch	2012, Ref. 48	HSQ	150/250	$>10^a$		<5	<0.5
		AZ4562	...	<10		70	1–50
		ma-N 2403	790	>3000		6	2–4
Pseudo-Bosch	2019, Ref. 61	HSQ	780–1850	>300		10	<6
		Al	200	>200		100	>10
		PS-NPs	<1400	200		2	<2
Pseudo-Bosch	2020, Ref. 59	Cr	~ 35	200	~ 34	100	1.5
		Cr_2O_3		200	~ 18		
		#PL-HAR	AZ5214E	~ 200	1000	~ 13	~ 100
Cryo-DRIE, this work	#NIL-HAR	UV Cur06	~ 300	~ 200 –800	~ 14	~ 120	>24
	#sub-100 nm-1	PS-NS	~ 460	~ 460	~ 44	>10	>1.8
	#sub-100 nm-2		~ 30	~ 200	~ 7	>667	>20
	#EBL-HAR	Cr	~ 30	30–1500	~ 50 –1	>667	1.5

^aHSQ resist of nanolines/nanostrips have been fabricated as masks, and “Si-NWs” in this work are Si-nanofins/nanosheets.

Selectivity referring to the etching of materials (Si) to a mask layer (resist or metal) is a further crucial figure of merit for etching high-aspect-ratio Si-NWs. Generally, for fluorine-based DRIE, metal masks have better selectivity over resist masks. Compared to the Bosch and the pseudo-Bosch processes, the drawback of using resist masks for cryo-DRIE is the limitation of resist thickness ($<1.5 \mu\text{m}$) owing to their cracking issue at cryogenic temperatures. Fortunately, the selectivity of Si etching to photoresist is greatly improved at these temperatures.³⁸ As shown in Fig. 6, when the etching time was increased that the Si has been etched to $\sim 20 \mu\text{m}$, the tops of the Si-NWs have been attacked, too, indicating that the 200-nm-thick photoresist mask (AZ5214E) has been completely etched away, resulting in an etching selectivity of ~ 100 . However, in our previous work,^{62,63} when AZ5214E resist is used for etching/releasing microcantilevers, Si of $\sim 300 \mu\text{m}$ in thickness, can be etched through using a 1- μm -thick resist mask (selectivity $> 300:1$). We assign the reduced selectivity to lateral etching, which is crucial to NWs due to their small lateral dimensions. In addition, we observed that with NIL resist (UV Cur06), a thickness of $\sim 200 \text{ nm}$ is required for etching Si-NWs of 400-nm-diameter to a height of $\sim 24 \mu\text{m}$, corresponding to a selectivity of ~ 120 [Fig. 4(a3)].

Both are much higher than the value of ~ 70 (resist AZ4562) reported in Ref. 38, using the pseudo-Bosch process for the fabrication of Si-NWs with diameters $> 3 \mu\text{m}$.

Both resist masks exhibited better selectivity at cryogenic temperature and are able to allow fabricating Si-NWs with higher aspect ratio than using the pseudo-Bosch process. In the case of a hard mask, a Cr layer of 30 nm in thickness has been employed. Here, the damage to the mask is virtually invisible after fabricating Si-NWs with a height of $\sim 20 \mu\text{m}$ (selectivity of Si:Cr $> 667:1$), revealing a much higher selectivity vs resist masks. Despite the large difference in the lateral etching rates (mask materials), the vertical etching rate is demonstrated to be independent of the mask materials. In addition, collapse and contamination, which are major challenges for liquid-phase fabrication techniques (e.g., MacEtch) in manufacturing dense Si-NWAs of high aspect ratio, have been avoided using cryo-DRIE. Selectivity values of typical mask materials used in our work and in references are calculated and summarized in Table II.

The systematic investigation of different lithography methods and mask materials and layouts resulted in specific cryo-DRIE recipes for yielding low mask undercut and high selectivity of silicon etching vs mask.

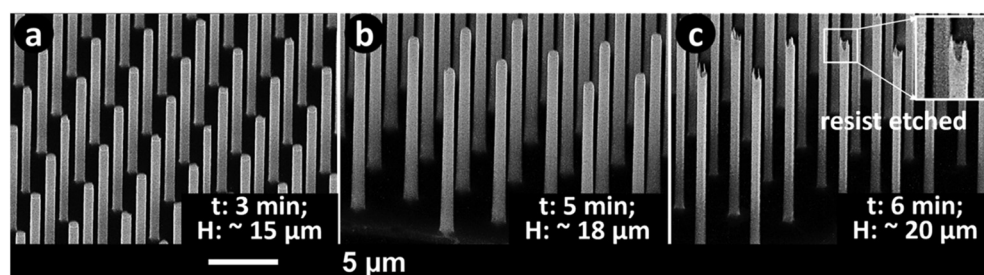


FIG. 6. SEM graphs of Si-NWAs of different heights (*H*) fabricated using cryo-DRIE (recipe: #PL-HAR, process parameters, see Table I) with patterned nanodiscs of photoresist AZ5214E ($D \sim 1200$ – $P4000$ – $H \sim 200$) as masks. The etching times *t* were (a) 3 min, (b) 5 min, and (c) 6 min. Inset of figure (c) is its partially magnified view, scale bar is $5 \mu\text{m}$, and *H* indicates the average heights of the Si-NWs.

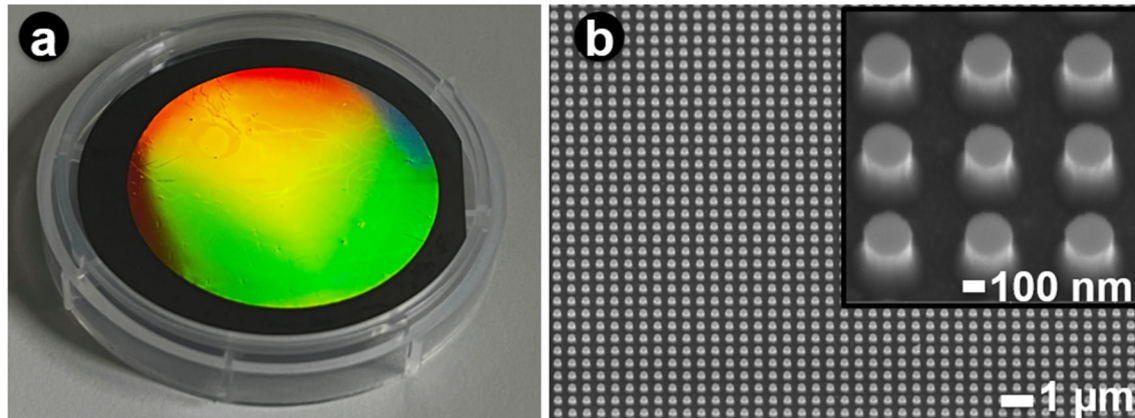


FIG. 7. Optical photograph (a) and 30° tilted-SEM graphs (b) of Si-NWAs (D~225-P500-H1600, for sample designation, see caption of Fig. 1) fabricated by cryo-DRIE (recipe #Nano-Uniformity, 5 min, process parameters, see Table I) using NIL resist (UV-Cur06, D~2500-P500-H~300)-masked 2-inch Si wafer ($\langle 111 \rangle$, 0.0005–0.001 $\Omega \times \text{cm}$). Inset of (b) is its partial-magnified view (30° tilted). Scale bars of figure (b) and its inset are 1 μm and 100 nm, respectively.

While lowest undercut was obtained with resist masks (PL and NIL), best selectivity was found with Cr patterned using EBL. Thereby, cryo-DRIE recipes using NIL and EBL are made available for micro pillars and NWs of heights of more than 20 μm . Using EBL highly ordered NWs of 30 nm in diameter and 1 μm in height were demonstrated.

B. Nanowire array profiles—uniformity and roughness

Due to its availability of offering uniform patterns of different NW size and area density on wafer scale as well as low undercut and high selectivity, NWs fabricated by cryo-DRIE (recipe #Nano-Uniformity, 15 min, Table I) of Si ($\langle 100 \rangle$, 1–10 $\Omega \times \text{cm}$), using resist masks prepared by NIL [design dimensions: D~400-P3200/4000-H~600 and D~250-P500H~300 (Fig. 7)] are employed for investigating uniformity and roughness of nanowire arrays (Si-NWAs). They have been characterized with respect to uniformity and fidelity of resulting NW dimensions using atomic force microscopy (AFM), scanning electron microscopy (SEM), angle-resolved Mueller matrix polarimetry (ARMMP), and angle-resolved Fourier microscopy (ARFM). AFM and SEM are predominately used with nanoscale features on small-scale area, while optical scatterometry methods, that can measure structures smaller than the used wavelength, can analyze periodic nanostructures on large scale, as preferred for industrial process metrology of large-scale, high-volume manufacturing.

1. Dimensional uniformity and fidelity of cryo-DRIE combined with NIL

First, a synergistic approach is adopted by combining AFM and SEM (Sec. IV C 1) to obtain a comprehensive dimensional characterization of the samples. AFM plays a crucial role in providing highly resolved information pertaining to the sample's height. However, it is worth noting that due to the convolution effect arising from the interaction between the AFM tip and the surface, AFM is limited in its ability to accurately measure lateral dimensions. On the other hand, SEM excels in offering detailed lateral resolution, providing valuable insights into the sample's structural features. However, SEM lacks quantitative information along the Z-axis. By integrating the capabilities of both

techniques, the limitations of each method can be overcome, allowing for a more complete understanding of the samples' dimensional characteristics. A set of ten SEM images was acquired for each sample with 11 NWs observable within the selected field (Fig. S7). The Mountains Lab[®] software (Digital Surf, France, Sec. IV C 1) was used to determine the NW pitch of each sample. The calculation is based on fast Fourier transformation. An example is given in Fig. 8, which shows an SEM graph of a hexagonal arrangement of circles characterized by two vectors \vec{a} and \vec{b} , oriented along the horizontal direction of the image and rotated by 60° clockwise to \vec{a} , respectively. A mean pitch is calculated together with a standard deviation by averaging $|\vec{a}|$ and $|\vec{b}|$ over the ten images. In addition, mean values and standard deviations of the

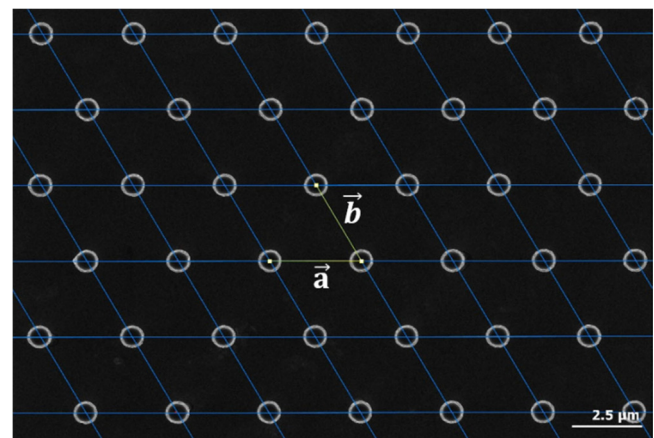


FIG. 8. Example of determination of the NWs pitches with fast Fourier transformation (FFT) tool (Mountains Lab[®], Digital Surf, instrumental details, see Sec. IV C 1), using SEM graph of Si-NWAs (D~800-P3200-H~1600) fabricated by cryo-DRIE (recipe #Nano-Uniformity, 15 min, Table I) with patterned nanodiscs of photoresist AZ5214E (D~800-P3200-H~300) as masks. The lattice highlighted on the image is a hexagonal arrangement of circles characterized by two vectors \vec{a} and \vec{b} , oriented along the horizontal direction of the image and rotated by 60° clockwise to \vec{a} , respectively. The scale bar is 2.5 μm .

TABLE III. Results for the pitch determination of samples (for sample designation, see caption of Fig. 1) fabricated by cryo-DRIE and NIL using SEM.

Sample name	$ \vec{a} /\mu\text{m}$	$ \vec{b} /\mu\text{m}$	Mean ($ \vec{a} , \vec{b} $)/ μm	Angle (\vec{a}, \vec{b})/ $^\circ$
D400-P3200-H1600	3.266 ± 0.002	3.143 ± 0.001	3.204 ± 0.001	59.22 ± 0.05
D400-P4000-H1600	4.080 ± 0.005	3.919 ± 0.006	3.999 ± 0.005	59.12 ± 0.05
D800-P3200-H1600	3.258 ± 0.001	3.138 ± 0.004	3.198 ± 0.002	59.22 ± 0.05
D800-P4000-H1600	4.088 ± 0.001	3.918 ± 0.004	4.003 ± 0.003	59.11 ± 0.05

angle between the two vectors are determined. The results of four layouts (NIL masks of D400/800-P3200/4000H300) are shown in Table III, with less than 0.13% in pitch deviation and less than 0.9° from the designed angle, indicating their wafer-scale uniformity and fidelity.

AFM (Sec. IV C 4) images of an area of $25 \times 25 \mu\text{m}^2$ were randomly captured on sample D400-P3200-H1600, with an image resolution of 1024×1024 pixels, corresponding to a pixel size of 24.4 nm . These two images contain a total of approximately 140 NWs. Figure 9 illustrates an example AFM image along with a magnified inclined 3D view. It is important to point out that the observed NWs appear triangular in their profile shape due to a convolution effect between the NW and the AFM tip. This effect is notable due to the similar sizes of the NWs and the AFM tip. However, since the top surface area of the NWs is expected to be flat and sufficiently large, convolution does not affect the measurements there, such as NW top-surface roughness and height. The height of the NWs is determined by analyzing the histogram of heights measured within the imaged 140 Si-NWs. The histogram exhibits two discernible peaks: the first peak corresponds to the height of substrate surface, while the second peak represents the top surface of the NWs (Fig. S8, green background and pink dots, respectively). By subtracting the maximum positions of these two peaks, a mean height of the NWs $1602 \pm 4.4 \text{ nm}$ is obtained, which is consistent with design and height measured by SEM ($\sim 1.6 \mu\text{m}$). The given expanded uncertainty (coverage factor, $k = 2$) includes an uncertainty that encompasses factors such as roughness, calibration, and repeatability (peak-to-peak value) and is only $\sim 0.3\%$ of the mean height of the NWs, confirming the etching uniformity of cryo-DRIE.

Modern patterning techniques like NIL offer delivering of NWAs on substrates of cm^2 to m^2 size at high throughput, which will require corresponding metrology tools. SEM and AFM can properly visualize form and dimensions of typically 10's of NWs of a VA-NWA on field of view (FOV) restricted to the μm range. Much larger FOV than SEM and AFM of typically 100's of μm to a few mm is provided by optical scatterometry,⁶⁴ effective medium approximation (EMA)-based Si-NWs evaluations of visible-near-IR ellipsometric measurements are fast and nondestructive method to determine both the thickness and porosity of mesoporous Si thin films and dense Si-NWs.⁶⁵ The typical spot size of optical scatterometry/ellipsometry yielding global information of an NWA is in the mm^2 range. For measuring local features of NWs, ellipsometry is combined with microscopy.⁶⁶ Such imaging-based scatterometry methods can reduce the time for measuring critical dimensions of nanoscale hourglass patterns on a 300 mm wafer from hundreds of days (with SEM or AFM) to several minutes.⁶⁷ Angle-resolved Mueller matrix polarimetry (ARMMP) uses a microscope objective of large numerical aperture,⁶⁸ enabling optical *in situ* characterization of Si-NWs at the initial growth stage of random Si-NWs.⁶⁹ Thereby, the light is focused on very small spots between $5 \mu\text{m}$ and few tens of μm in diameter and the light from a wide range of incidence and azimuthal angles is collected at once. Thus, the formation of domains with different 2D arrangement of Si-NWs can be detected, which is typical to VA-Si-NWAs fabricated by NSL and MacEtch.⁶⁸ Within the domains, i.e., on a short-range scale, the NWs were ordered in hexagonal arrays as expected from the NSL mask pattern. Moreover, the rather recently reported technique of spectral domain

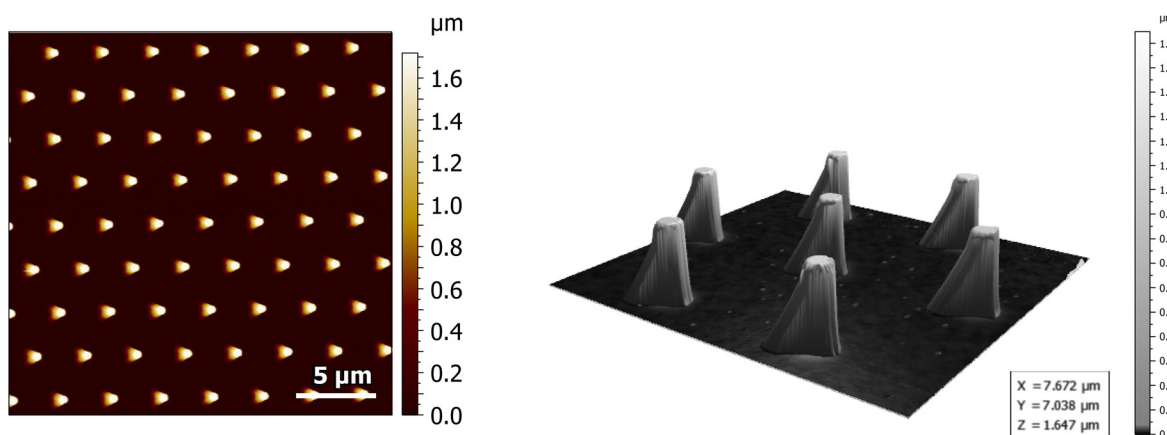


FIG. 9. Left: Atomic force microscopy (AFM) image (top view, the scale bar is $5 \mu\text{m}$) of Si-NWAs (D~400-P3200-H~1600, for sample designation see Fig. 1) fabricated by cryo-DRIE (recipe #Nano-Uniformity, 15 min), using patterned nanodiscs of NIL resist (D400-P3200-H300). Right: a representative detail-magnified inclined 3D view of this identical sample. The color bar indicates the sample surface height.

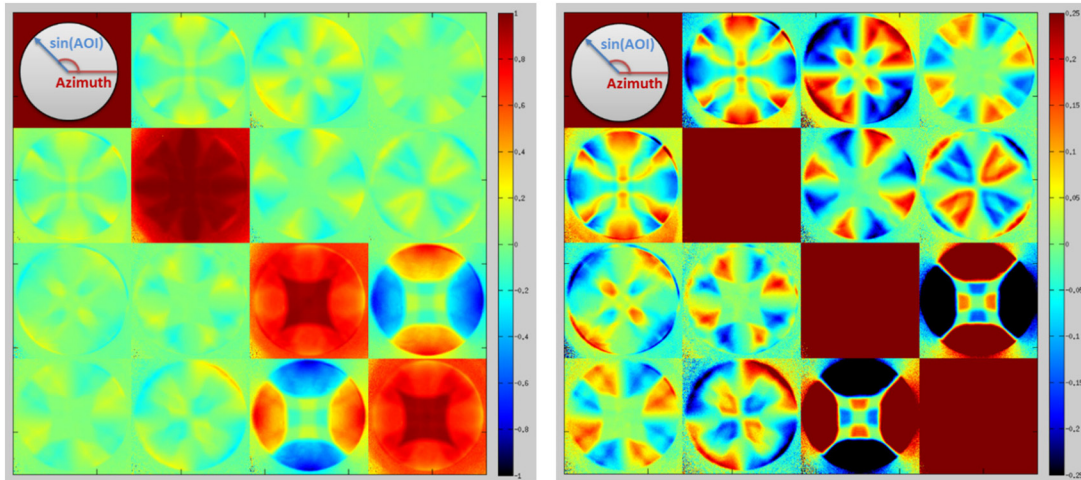


FIG. 10. Left: Normalized measured Mueller matrix (MM) elements of Si-NWAs sample (D225-P500-H350, for sample designation see Fig. 1) fabricated by cryo-DRIE (recipe #sub-100 nm-2, 8 min, process parameters see Table I) using nanodiscs of NIL resist (UV Cur06, D250-P500-H~300), with a scale from -1 to 1 for each matrix element. Each square represents one of 16 MM elements. Right: The same measurement plotted with a scale of -0.25 to 0.25 to show more details in the off-diagonal matrix elements (AOI: angle of incidence). The measured area amounts to about $60 \times 60 \mu\text{m}^2$.

attenuated reflectometry is not only used to quantify the surface density, but also to assess the lateral gradients of non-homogeneous nanowire arrays (e.g., ZnO-NWs).^{70,71}

In this study, angle-resolved Mueller matrix polarimetry (ARMMP) measurements (Sec. IV C 2) were performed on a periodic nanowire array (Si-NWA) with a pitch of 500 nm (Fig. 7, D225-P500-H350, for sample designation, see caption of Fig. 1) was taken at wavelength of 550 nm using an objective numerical aperture of 0.9 as shown in Fig. 10. The circles in Fig. 10 show all 16 elements of the Mueller matrix (MM, color) as a function of sine of the angle of incident (AOI, from the center to the outside) and the azimuthal angle. Due to the use of an objective, the images are circular with the circle edge being the numerical aperture of the objective. The pixels close to the circle center correspond to normal incidence where clearly only specular light has been collected. Regions with strong signal are shown in the matrix element M_{34} in Fig. 10 (right) obtained from the specular beam mixed with the diffraction orders, creating a distinct pattern in the left, right, top and down part of the image. The configuration of the diffraction orders is defined by the square periodicity of the Si-NWA (see Fig. 7), which means that there are nine visible diffraction orders $[-1, -1]$ $[0, -1]$ $[1, -1]$ $[-1, 0]$ $[0, 0]$ $[1, 0]$ $[-1, 1]$ $[0, 1]$ $[1, 1]$. The pattern formed by these diffraction orders is a 3×3 grid with equidistantly distributed nine circles (shifted by wavelength to period ratio), each overlapping with the central circle $[0, 0]$ and with the closest neighbors. Higher orders than first are not observed in the measurement as the period-to-wavelength ratio is higher than one. The more detailed images in Fig. 10 (right) show complex patterns reflecting the optical response from the overlapping diffraction orders of the periodic Si-NWA. A rigorous optical model is required to calculate the depolarizing character of the measured MMs quantitatively. Nevertheless, the position of the diffraction orders and the (anti-)symmetry of the off-diagonal MM elements already visible here confirm the high uniformity and fidelity of the periodic symmetric square arrangement of the fabricated NWs in the measured area of about $60 \times 60 \mu\text{m}^2$. This result is remarkable with respect to earlier ARMMP measurements with

VA-Si-NWAs by NSL and MacEtch, where ordered NWs were observed in domains of much smaller scale ($< 5 \mu\text{m}$).⁶⁸

Beyond such a qualitative evaluation, more quantitative information about the dimensions of NWs in an array can be obtained by combining fast in-line optical metrology tools with off-line SEM and/or AFM measurements.⁵⁴ In this context, angle-resolved Fourier microscopy (ARFM) was done with Si-NWAs of 500 nm pitch fabricated by EBL and cryo-DRIE in Fig. 11. Here, Fourier scattering-diffraction efficiencies were obtained applying a smaller wavelength (488 nm) than given by the period (500 nm) of the measured structure. Therefore, the diffraction pattern is characteristic due to the large number of diffraction orders included within the numerical aperture (0.9) of the scatterometer. The calculated model scattering-diffraction efficiencies η^c in Fig. 11(b) (see Sec. IV C 3) were generated for the χ^2 -plot with a minimum for the parameters of height of 205 nm and diameter of 110 nm in Fig. 11(c). The measured AFM height was found to be $204 \pm 2 \text{ nm}$.⁷² Small differences between the measured and simulated images are observed, which we relate to not perfectly uniform dimensions of the NWs across the field of view of approximately 0.25 mm in diameter. The χ^2 -plot reveals that the diameter can be found with small uncertainty, whereas the height uncertainty is much larger. This is confirmed by the estimated average uncertainties calculated from the covariance matrix, which yield a height uncertainty of 1.3 nm and a width uncertainty of 0.2 nm . We therefore believe that the main contribution to the observed difference between simulated and measured diffraction efficiencies is due to height variations of the structure. A non-zero correlation coefficient between height and diameter is found (-0.3), which means that a change in one parameter p^c will be partly counteracted by the other.

2. Characterization of roughness

To investigate the sidewall roughness of the NW, a nanomanipulator, kindly provided by the company Kleindiek (Reutlingen, Germany), was installed in a combined AFM-SEM (FusionScope™)

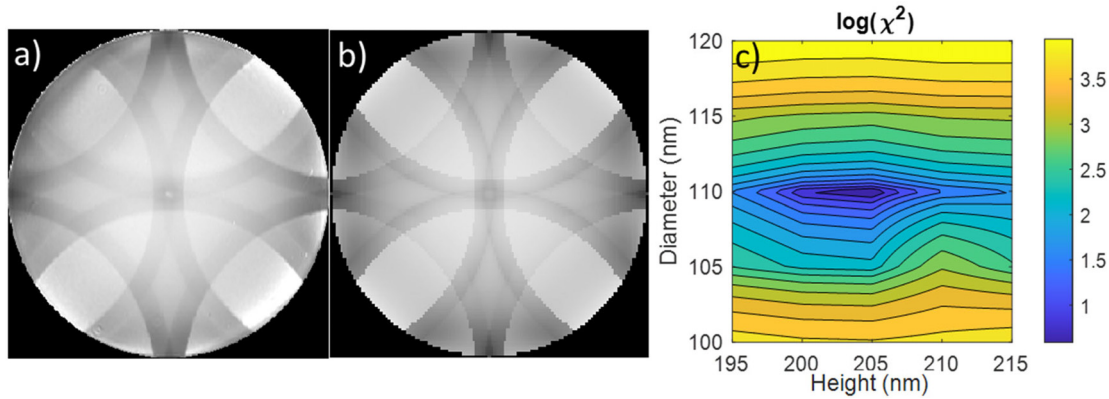


FIG. 11. (a) Measured Fourier scattering-diffraction efficiencies, (b) simulated diffraction efficiencies, and (c) χ^2 -plot around the minimum in the diameter-height space. All experiments have been performed with Si-NWAs of 500 nm pitch fabricated by EBL and cryo-DRIE (D \sim 100P500H \sim 200, recipe #sub-100 nm-2, 5 min) (for sample designation, see Fig. 1) for an image size of 640×480 pixels using unpolarized light at 488 nm. The field of view had a diameter of approximately 0.25 mm, i.e., it contains $\sim 2.5 \times 10^5$ NWs.

and was used to crack free-standing NWs at their base (Sec. IV B 5). NWs (D1200-P1600-H \sim 20000, for sample designation, see Fig. 1) have been fabricated by cryo-DRIE (recipe #NIL-HAR, 5 min, Table I) of Si ($\langle 100 \rangle$, 1–10 $\Omega \times \text{cm}$) and NIL masks [Fig. 5(a1)] have been used in this experiment. The combination of AFM and SEM in one system enables a user to easily find a cracked NW [see Fig. 12(a)], to precisely navigate the AFM tip to a specific position on the NW, and finally to perform high-resolution AFM measurements there. The red rectangle in the SEM image of Fig. 12(a) indicates the position, where the AFM measurement shown in Fig. 12(b) has been performed. To analyze the sidewall roughness in more detail, a zoomed-in image of the sidewall is displayed in Fig. 12(c) as well as an extracted height profile [Fig. 12(d)]. The analysis of the studied NW revealed a sidewall roughness of approximately 13 nm (RMS value).

To study the properties of the NWs such as diameter, height, pitch, and surface roughness, NWs (D40-1500P500-1500H290), prepared by cryo-DRIE (recipe #sub-100 nm-2, 7 min, Table I) of Si ($\langle 111 \rangle$, 54–66 $\Omega \times \text{cm}$) and EBL-Cr masks, have been investigated with the FusionScopeTM. To this end, the SEM function has been used to find

an arbitrary NW on the sample [see Fig. 13(a)], which has been selected to perform high-resolution AFM measurements [Sec. IV C 5]. Figure 13(c) displays a 3D representation of the topography of the selected NW. The height profile extracted from the AFM image shown in Fig. 13(d) reveals a NW height of approximately 290 nm and a diameter of approximately 1.5 μm , which fits well to the targeted NW diameter (1500 ± 20 nm). The NW-top-surface roughness and the bottom-space-surface roughness have been analyzed from the zoomed-in AFM images shown in Figs. 13(e) and 13(f), respectively. A NW top-surface roughness of approximately 0.3 nm has been measured, indicating the top of Si-NWs has been well protected from etching by the Cr mask. The bottom-space-surface roughness of approximately 2 nm of the etched Si at the bottom can be considered as smooth, too (see Table IV). For comparison, top- and bottom-roughness levels of sample D400P3200H1600 (Recipe #Nano-Uniformity, 15 min) have been measured by AFM (Fig. S9), resulting in a measured roughness (RMS) values of 3.4 ± 0.3 and 2.7 ± 0.5 nm at the top surface of the NWs and bottom surface in between (Tables SIII and IV), respectively. It has to be noted that, here, roughness is measured by scanning over many

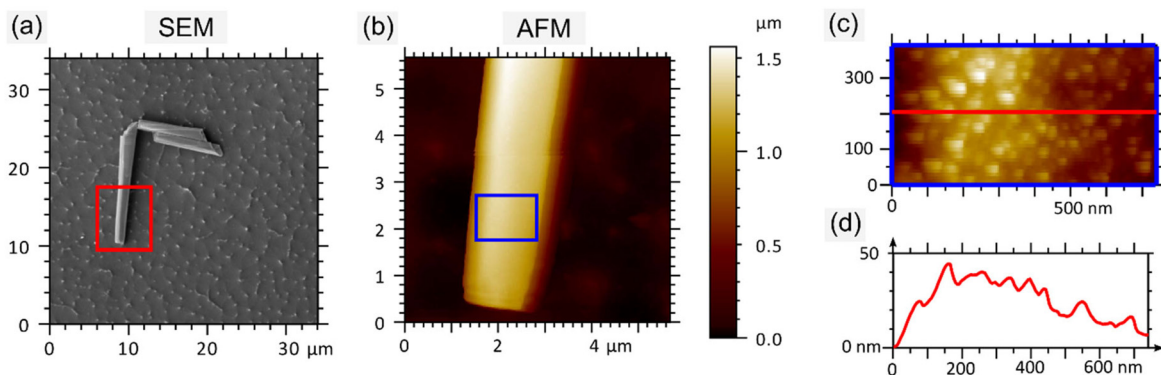


FIG. 12. (a) SEM top view of a NW sidewall (recipe #NIL-HAR, 5 min, Table I) (for sample designation see Fig. 1). The red rectangle indicates the measured area, in which the AFM image shown in (b) has been recorded. (b) AFM topography of the NW sidewall. (c) Zoom-in image of the NW shown in (b) (indicated by the blue rectangle). (d) Corresponding height profile along the red line in (c).

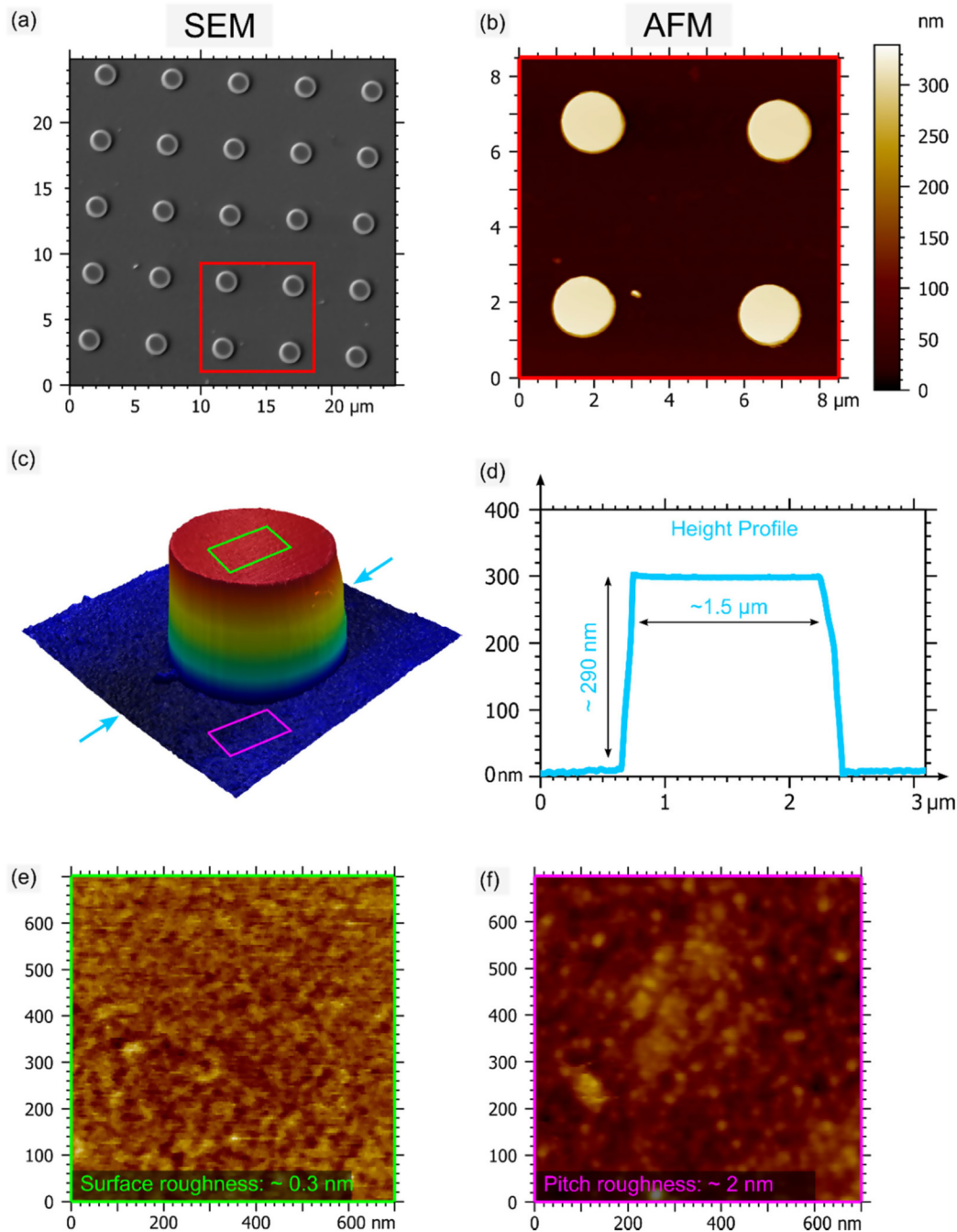


FIG. 13. (a) SEM top view of a Si-NWAs (D1500-P5000-H290) (for sample designation see Fig. 1) fabricated by cryo-DRIE (recipe #sub-100 nm-2, 7 min, Table I), using nano-discs of Cr (D1500-P5000-H30) prepared by EBL. The red rectangle defines an arbitrary area, where an AFM image (b) was subsequently recorded. In (c), a 3D representation of the topography of one NW is depicted with blue arrows indicating the starting and ending point of an extracted height profile displayed in (d). The green and magenta rectangles in (c) correspond to the areas, where the images (e) and (f) are recorded to investigate the bottom and NW-top-surface roughness.

NWs along bottom-sidewall-top surfaces. Therefore, the undercut induced “roughness” has been measured (3.4 nm). Here, since its top has been protected from etching by masks, its roughness is consistent ~ 0.3 nm confirmed by FusionScope™.

Topography and surface roughness of NWAs were imaged both on small scale containing about 10 NWs using SEM and AFM and on large scale with up to $\sim 2.5 \times 10^5$ NWs using optical scatterometry (ARFM). A combination of AFM and ARFM in a hybrid metrology

TABLE IV. Summary and comparison of fabricated of Si-NWAs artifacts. n.m.: not measured; n.a.: information is not available in references.

Material	Recipe	Crystallographic orientation	Etch rate ($\mu\text{m}/\text{min}$)	Aspect ratio	Diameter (nm)	Top/bottom/sidewall roughness (nm)	Height (μm)
Cryo-DRIE	#EBL-HAR	$\langle 111 \rangle$	~ 4	> 100	> 200	n.m./n.m./n.m.	> 20
	#sub-100 nm-2	$\langle 111 \rangle$	0.07	> 30	> 10	$\sim 0.3/\sim 2/\text{n.m.}$	> 0.35
	#NIL-HAR	$\langle 100 \rangle$	~ 4	> 60	> 400	$3.4 \pm 0.3^a/2.7 \pm 0.5/\sim 13$	> 24
Cryo-DRIE & PEO	#PL-HAR & $3 \times$ PEO	$\langle 100 \rangle$	~ 4	~ 80	~ 230	n.m./n.m./n.m.	18
	2023, Ref. 3	$\langle 100 \rangle$	n.a.	~ 2	> 230	n.a./ $> 10/\text{n.a.}$	< 0.5
Bosch process	2018, Ref. 42 ^b	n.a.	n.a.	> 50	~ 1000	n.a./n.a./ $\sim 507 \pm 40$.	~ 50
	2019, Ref. 46	n.a.	3–5	120	500	n.a./10/n.a.	60
	2012, Ref. 48	$\langle 100 \rangle$	< 0.36	~ 50	< 10	n.a./smooth/n.a.	< 0.5
SDRIE	2011, Ref. 47	n.a.	0.18	58	24	n.a./smooth/n.a.	1.39
Pseudo-Bosch	2019, Ref. 38	$\langle 100 \rangle$	0.4–0.5	> 50	> 200	n.a./n.a./n.a.	10–14
Gas-MacEtch	2023, Ref. 35	$\langle 100 \rangle$	0.3–0.5	200	200	n.a./1–5/ n.a.	43

^aHere, the undercut has been included in the given value, POE: post-etching oxidation.

^bThe process temperature of the Bosch process was approximately -19°C (minimum allowed by their tool).

approach, which can yield diameter, pitch, and height at low uncertainty, showed high uniformity and fidelity of cryo-DRIE-fabricated Si-NWAs close to the mask design using NIL and EBL. Very low roughness in the nm range or even below was found on top and at the bottom of the NWs, and the sidewall roughness was ~ 13 nm.

C. Process-parameter variation

To investigate and explain how process parameters affect profile, morphology, and height (etch rate) of the obtained NWs, recipes #Nano-Uniformity and #EBL-HAR (Table I) are used as benchmarks for etching Si of various crystal orientations and doping concentrations with masks of different layout designs. The impacts of process parameters are checked by controlled variables and visualized by SEM graphs. Since its availability of offering uniform patterns on wafer scale [Fig. 7(a)] and good sticking efficiency as well as high selectivity, resist masks prepared by NIL (D \sim 400-P \sim 3200/ \sim 4000-H \sim 600) are employed for investigating the effect of cryo-DRIE process parameters to the morphology of etched Si-NWAs. For these experiments, if not specified, wafers of Si $\langle 100 \rangle$ (phosphorus-doped, $1\text{--}10 \Omega \times \text{cm}$, $4''$) are applied.

1. Gas concentration and flow rates

A straight and smooth sidewall profile is generally expected and required for high-aspect-ratio Si-NWAs, but a sloped sidewall angle and a smooth sidewall topography are preferred for water/oil repelling surfaces and through Si via (TSV) applications. For all desired morphologies, profile control is critical, which is determined by the ratio of etching and passivation. As mentioned above, in SF_6/O_2 gas mixtures, the fluorine radicals are destined to etch the Si, whereas the oxygen radicals are used to form the SiO_xF_y passivation layer to protect the Si-NWAs sidewalls from being etched, so as to achieve a good control of the etching profile. Etching Si-NWAs with vertical sidewall profile can be realized at a SF_6/O_2 gas-flow ratio where etching and passivation equilibrium is achieved.

Influences of gas concentration have been investigated by increasing the percentage of O_2 of the total gas flow from $\sim 2\%$ to $\sim 14\%$, i.e.,

the O_2 flow rate has been increased from 2 to 10 sccm, with the flow rate of SF_6 fixed at 60 sccm [Figs. 14(a)–14(c)] and varied from 80 to 120 sccm [Figs. 14(d) and 14(f)]. The other process parameters were fixed (recipe #Nano-Uniformity, 10 min, Table I). Theoretically, an increased O_2 concentration leads to a decrease in the etch rate and a positive-tapered profile due to faster formation of the passivation layer, which is confirmed by the results shown in Figs. 14(b), 14(c), 14(e), and 14(f), whereas, for O_2 concentration at $\sim 3\%$ [Fig. 14(a)] and $\sim 2\%$ [Fig. 14(d)], only pyramidal nanostructures have been observed. This is because of the collective effect of high etch rate and low passivation-forming rate, inducing a formation of inverse cones rather than NWs, which topple down and are subsequently etched from the sidewall. To confirm this suspicion, a 30-nm-thick Cr mask has been used instead of a resist mask to repeat the etching. After etching for 5 min, toppled-down Si-NWAs with Cr disks on their tops can be observed [Fig. S10(a)], and with increasing etching time, “lying-flat Si-NWAs” have been etched from their sides, leaving Cr-mask flakes and residual pyramid-shape bases [Fig. S10(b)]. Based on this observation, we can conclude that as the concentration of O_2 increases, the etch rate reduces notably and the tapered angle turns markedly from negative to positive.

In addition, changing gas-flow rates at fixed SF_6/O_2 ratio has been investigated, by comparing Figs. 14(b)–14(e) ($\text{SF}_6/\text{O}_2 = \sim 91\%:9\%$) and Figs. 14(c)–14(f) ($\text{SF}_6/\text{O}_2 = \sim 86\%:14\%$), respectively. The vertical etch rate is measured to be independent of flow rates, resulting in ~ 140 and ~ 73 nm/min at SF_6/O_2 of $\sim 91\%:9\%$ and $\sim 86\%:14\%$, respectively. On the contrary, diameters of NWs fabricated at high gas-flow rate are measured to be smaller than those at lower rate, which are ~ 530 [Fig. 14(e)] to ~ 660 nm [Fig. 14(b)] and ~ 620 [Fig. 14(f)] to ~ 760 nm [Fig. 14(c)], indicating that the NWs have been more laterally etched at high gas-flow rate. However, when the etch rate has been increased by using a higher ICP power (recipe #NIL-HAR, Table I), we find that at too-low gas-flow rate ($\text{SF}_6/\text{O}_2 = 30$ sccm:2.8 sccm $= \sim 91\%:9\%$) black Si is created [Fig. S11(a)]. Even at a similar gas-flow rate as used for recipe #Nano-Uniformity (Table I), the NWs sidewalls are still rough, while increasing the gas-flow rate to $\text{SF}_6/\text{O}_2 = 120$ sccm:11 sccm brings about smooth etching [Fig. S11(c)]. Therefore, for fabricating high-aspect-ratio Si-NWAs with high etch rates, gas-flow rates higher than 100 sccm are preferred.

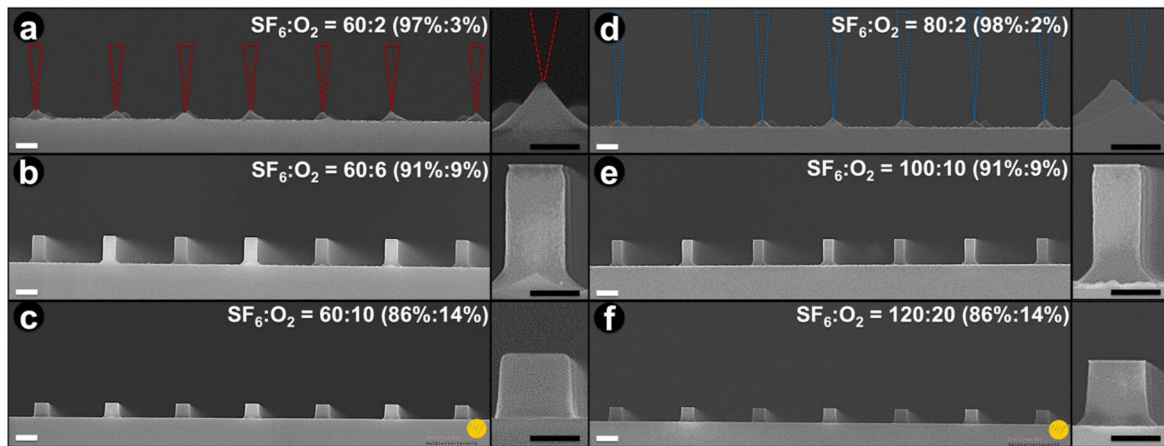


FIG. 14. Cross-sectional SEM graphs of Si-NWAs etched at different gas-flow rates (given in sccm) by cryo-DRIE using patterned nanodiscs of NIL resist ($D \sim 400\text{-P} \sim 3200\text{-H} \sim 600$) as masks, with the other cryo-DRIE parameters fixed [(a)–(f): recipe #Nano-Uniformity, 10 min, Table I]. The figures on the right sides exhibit magnified views of single NWs. Dashed red and blue lines in (a) and (d), respectively, indicate Si-NWAs of negative-tapered profile before toppled-down (not to the real scale). The scale bars are 1000 nm (white) and 300 nm (black), respectively. The resist masks were removed after etching of Si-NWAs.

The morphology of the obtained NWs is correlated with the mask layout at fixed processing parameters, as we mentioned before. Taking advantage of the high resolution and layout-design flexibility of EBL, 30-nm-thick Cr-mask nanodiscs with different diameters and pitches have been fabricated. As shown in Fig. 15, the etch rate of Si is measured to be almost the same (~ 75 nm/min) for the different layouts, resulting in Si-NWAs with aspect ratios of ~ 16 [Fig. 15(a)], ~ 15 [Fig. 15(b)], and ~ 7.5 [Fig. 15(c)], respectively. Furthermore, their profile angles (angle of sidewall with respect to bottom surface) are found to be close to the same value ($\sim 85.5^\circ \pm 0.4^\circ$) as well, i.e., this observed uniformity indicates that an influence of the etching-loading effect⁵¹ to the layout design is not visible, which is different to trench etching.

For etching Si-NWAs of high aspect ratio, precise control of gas concentrations at high flow rate is crucial; therefore, the relation between NW morphology and layout design has been experimentally investigated with Si-NWAs of various diameters and pitches using numerous recipes for cryo-DRIE. Representative results are shown in Fig. 16, wherein the vertical etch rate is approximated to be the same for different patterns of Si-NWAs of ~ 20 μm in height (aspect ratio < 100). The profile angle of the Si-NWAs keeps constant, which is confirmed by

Fig. 16, as well as Figs. S9–S11, where the profile angles at the NWs' bottom part amount to $\sim 98.3^\circ \pm 0.4^\circ$ [D300-P1000H20000, Fig. 16(a)], $\sim 98.2^\circ \pm 0.3^\circ$ [D500-P1250-H20000, Fig. 16(c)], and $\sim 98.2^\circ \pm 0.4^\circ$ (D800-P2500H20000 to D1300-P2500-H20000, Figs. 16(f) to 16(j)). Compared to the Si-NWAs shown in Fig. 15, there are much larger undercuts observed than for the Si-NWAs shown in Fig. 16. This is attributed to the larger ICP power resulting in larger etch rate at the beginning of etch, when the formed passivation layer is not thick enough to protect the sidewall. Therefore, for the Si-NWAs with diameters smaller than 200 nm, masks dropped from their tops and the Si-NWAs have been etched. These etching phenomena can be further confirmed by changing the gas concentrations as shown in Figs. S12 and S14, wherein the profiles turn gradually from negative to positive as the O_2 concentration increases from $\sim 10\%$ (Fig. S12) to $\sim 11.5\%$ (Fig. S13), and $\sim 14.6\%$ (Fig. S14). Here, the cryo-DRIE recipe #EBL-HAR (Table I, 5 min) is used, with the total gas flux and other parameters fixed.

In addition, for all samples, the Si-NWAs located at the edges of an array have either more negative (Fig. S12) or positive (Figs. S15 and S16, depending on the recipes) profiles with respect to the Si-NWAs from inside an array. These irregular shapes are induced by a collective

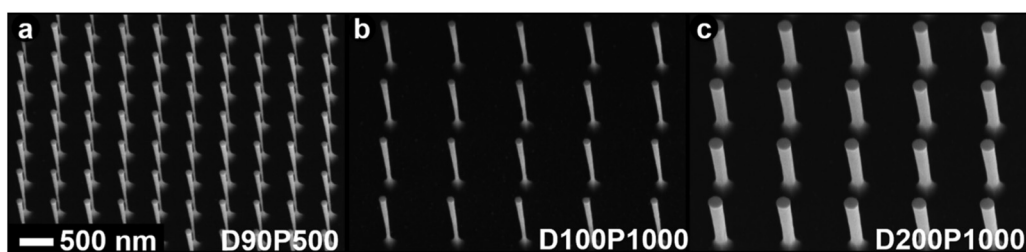


FIG. 15. 30° tilted-SEM graphs of Si-NWAs fabricated by DRIE (#sub-100 nm-1, 20 min, process parameters; see Table I) using nanodiscs of Cr (30 nm in thickness) patterned by EBL with different mask layouts as masks, on $1 \times 1 \text{ cm}^2$ Si ($\langle 111 \rangle$, $0.0005\text{--}0.001 \Omega \times \text{cm}$). (a) $d_{\text{NW}} \approx 90$ nm, pitch ≈ 500 nm, height ≈ 1490 nm; (b) $d_{\text{NW}} \approx 100$ nm, pitch ≈ 1000 nm, height ≈ 1488 nm; (c) $d_{\text{NW}} \approx 200$ nm, pitch ≈ 1000 nm, height ≈ 1500 nm. The Cr masks were removed after etching of the Si-NWAs. The scale bar is 500 nm for all samples.

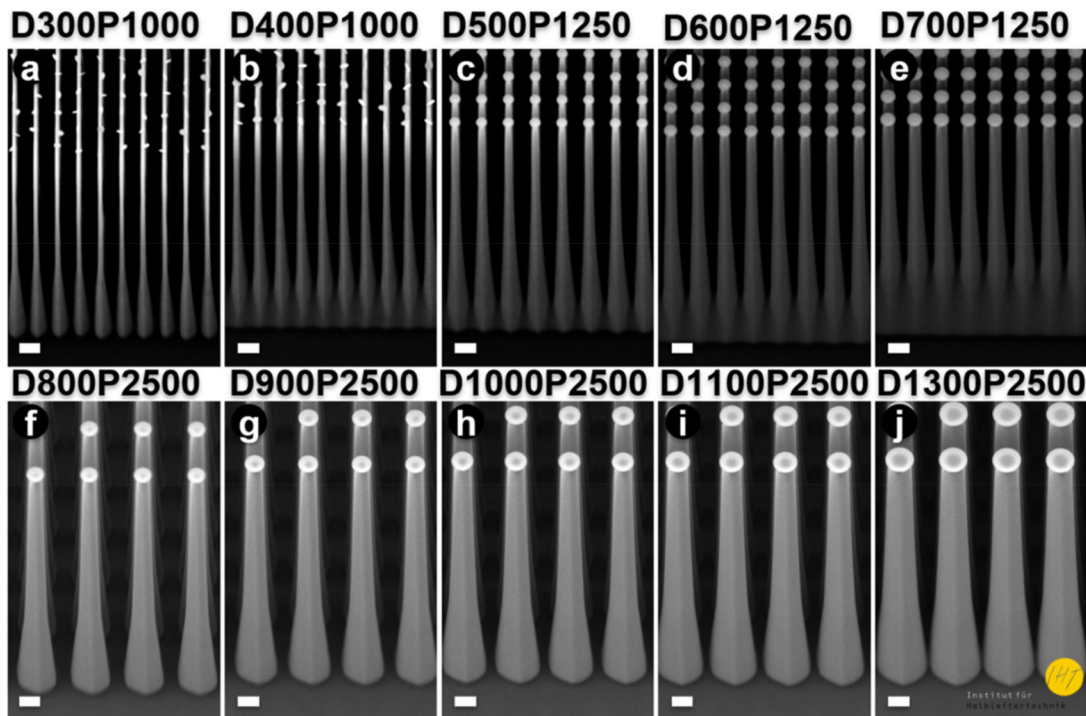


FIG. 16. 30° tilted-SEM graphs of Si-NWAs fabricated by cryo-DRIE (recipe #EBL-HAR, $\text{SF}_6:\text{O}_2 = 115 \text{ sccm}:15 \text{ sccm} = \sim 88.5\%:11.5\%$, 5 min, with other process parameters fixed, see Table I) using nanodisks of Cr (30 nm in thickness) of different diameters (D: 300–1300 nm) and pitches (P: 1000, 1250, and 2500 nm, Fig. S5 and Table S2) (a) $d_m \approx 300 \text{ nm}$, pitch $\approx 1000 \text{ nm}$; (b) $d_m \approx 400 \text{ nm}$, pitch $\approx 500 \text{ nm}$; (c) $d_m \approx 500 \text{ nm}$, pitch $\approx 1250 \text{ nm}$; (d) $d_m \approx 600 \text{ nm}$, pitch $\approx 1250 \text{ nm}$; (e) $d_m \approx 700 \text{ nm}$, pitch $\approx 1250 \text{ nm}$; (f) $d_m \approx 800 \text{ nm}$, pitch $\approx 2500 \text{ nm}$; (g) $d_m \approx 900 \text{ nm}$, pitch $\approx 2500 \text{ nm}$; (h) $d_m \approx 1000 \text{ nm}$, pitch $\approx 2500 \text{ nm}$; (i) $d_m \approx 1100 \text{ nm}$, pitch $\approx 2500 \text{ nm}$; and (j) $d_m \approx 1300 \text{ nm}$, pitch $\approx 2500 \text{ nm}$, patterned by EBL as masks on $1 \times 1 \text{ cm}^2$ Si ($\langle 111 \rangle$, $0.0005\text{--}0.001 \Omega \times \text{cm}$). The scale bar is 1000 nm, and Cr disks have not been removed. For sample designation, see caption of Fig. 1, here NW height amounts to $H = 20 \mu\text{m}$.

effect of feature-size-dependent loading and aspect-ratio-dependent etching (ARDE, also known as the etch lag in RIE). When the process begins, the “macro-surface” around the Si-NWAs is etched indistinguishably from the interior of the Si-NWAs (Fig. 15), i.e., there are sufficient radicals traveling among the NWs. As etching progresses, the difference of generating NWs to trenches⁵¹ becomes notable, since $> 75\%$ of the Si bulk have been etched to create Si-NWAs, which is much more than that ($< 10\%$) involved for uniform trench etching.⁷³ Therefore, the reactants are consumed faster during NW etching than for trench etching, leading to lower etch rate and uniformity. For example, the profile angle of NWs is more sensitive to small space than the mask/space ratio, which means that passivation rate exceeds etching rate. Either the fluorine radicals can only penetrate more difficult through the small gaps, or the SiF_4 reaction product is released less easily to the top surface. The Si-NWAs close to the macro-surface are better accessible and therefore can be etched easier than the interior region (Figs. S15 and S16). Similarly, with increasing Si-NWAs’ height, the reactants need to diffuse through the already etched structures in order to support a constant etching rate at the bottom. Therefore, again, passivation exceeds etching and the profile angles gradually turn to more and more positive until the wires merge into each other at their bases (Figs. 16 and S13). However, such irregular Si-NWAs are observed only among the outermost edges of the arrays when fabricating Si-NWAs of ~ 100 aspect ratio, which is negligible on the wafer

scale. In a further experiment, as shown in Fig. S14, etching has been interrupted and the sample has been brought back to room temperature and pressure before a second cycle of etching has been continued. Here, it can be observed clearly that the second etching has started as in the first run, both in lateral and vertical directions, leading to a two-part frustum, the upper part of which has a smaller diameter than the lower, due to a loss of its passivation layer during the process interrupt. Different to the pseudo-Bosch process, wherein the passivation layer on the surface of Si-NWAs has to be removed after the fabrication of Si-NWAs, the SiO_xF_y passivation layer generated in cryo-DRIE evaporates by itself during the warming-up of the chamber to room temperature. No cleaning procedure is required after cryo-DRIE to end up with NWs of very clean and smooth sidewall surface.

2. Temperature

Notable results are observed for experiments at different etching temperatures T (Fig. 17). Higher etching temperature resulted in the fabrication of higher bowling-shaped Si-NWAs with negatively tapered profiles, using recipe #Nano-Uniformity (Table I). The etch rate at -85°C [Fig. 17(a)] exceeds that at -120°C [Fig. 17(d)] by more than fivefold, specifically 240 nm/min compared to 45 nm/min . Additionally, at higher temperatures, the etching undercut is more pronounced than that observed in Si-NWAs obtained at lower

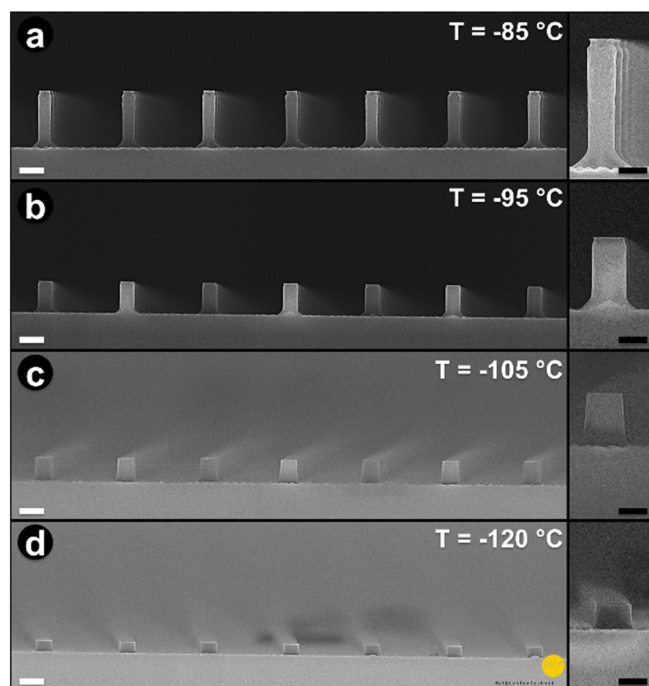


FIG. 17. Cross-sectional SEM graphs showing the influence of etching temperature T on the fabrication of Si-NWAs using cryo-DRIE (recipe #Nano-Uniformity, 10 min, with the other process parameters fixed, process parameters; see Table I) and patterned nanodiscs of NIL resist ($D\sim 400\text{-}P\sim 3200\text{-}H\sim 600$) as masks, (a) temperature at -85°C , (b) temperature at -95°C , (c) temperature at -105°C , and (d) temperature at -120°C . Magnified views of corresponding single NWs are displayed on the right. The scale bars (white/black) correspond to $1\ \mu\text{m}/500\ \text{nm}$. The resist masks were removed after etching of Si-NWAs.

temperatures. Both the heightened etch rate and increased undercut can be attributed to the enhanced reactivity of radicals at elevated temperatures. For the achievement of Si-NWAs with precise morphology, it is imperative to maintain the etching temperature within the range of -105°C to -95°C [Fig. 17(c)]. Within this temperature range, the sidewalls exhibit a notably smoother appearance. Furthermore, Si-NWs etched at -95°C with an ideal profile angle of $90.0^\circ \pm 0.05^\circ$ offer a superior opportunity for profile fine-tuning by adjusting other etching parameters compared to those etched at -105°C (profile angle $93.7^\circ \pm 0.3^\circ$). Especially when etching large-scale or high-aspect-ratio (HAR) Si-NWAs, a temperature of -95°C is preferred over -105°C due to its higher etch rate. At -95°C , the etch rate reaches approximately $145\ \text{nm}/\text{min}$, in contrast to around $90\ \text{nm}/\text{min}$ at -105°C , as illustrated in Fig. 17(c). To ensure that the temperature of the sample surface during etching corresponds to the indicated electrode temperature, good thermal contact between sample and the stainless-steel holder is essential. In our experiments, thermal-conductive grease (fomblin oil) has been applied between the backside of the sample and the sample holder.

3. ICP power

ICP power determines the concentration of ion/radical density available for isotropic chemical etching, as indicated in Figs. 18(a)–18(c).

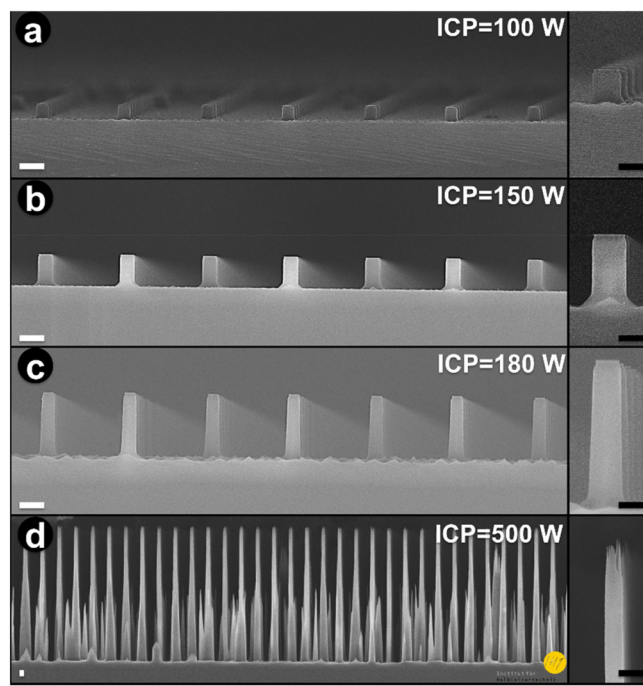


FIG. 18. Cross-sectional SEM graphs showing the influence of ICP power on the fabrication of Si-NWAs using cryo-DRIE (recipe #Nano-Uniformity, 10 min, with the other process parameters fixed, process parameters; see Table I) and patterned nanodiscs of NIL resist ($D\sim 400\text{-}P\sim 3200\text{-}H\sim 600$) as masks, (a) ICP power at $100\ \text{W}$, (b) ICP power at $150\ \text{W}$, (c) ICP power at $180\ \text{W}$, and (d) ICP power at $500\ \text{W}$. Magnified views of corresponding single NWs are displayed on the right. The scale bars (white/black) correspond to $1\ \mu\text{m}/500\ \text{nm}$. The resist masks were removed after etching of the Si-NWAs.

Correspondingly, the vertical etch rate increases from ~ 65 to $\sim 270\ \text{nm}/\text{min}$, when the ICP power is increased from 100 to $180\ \text{W}$. Increasing the ICP power further to $500\ \text{W}$ with the other process parameters fixed aggravates the surface roughness and leads finally to an evolution of black Si, as shown in Fig. 18(d). Simultaneously, the diameter of the Si-NWAs decreases from ~ 600 to $\sim 500\ \text{nm}$, revealing enhanced lateral etching. If the ICP power is increased further from 300 to $700\ \text{W}$, as we can observe in Fig. S17, the profile of the NWs turns from positive-tapered to negative-tapered, evidencing a weakened formation rate of the passivation layer compared to the fluorine-radical-dominated Si etching. This means that the F^* concentration has been enhanced over the O^* concentration by increasing the power/ion density.

4. RF power

The RF power parameter controls the ion energy, which is manifested as the density of directional irradiation of the sample by ions and dragged radicals. Therefore, the value of RF power determines the removal of the SiO_xF_y passivation layer from bottom surface by increasing the kinetic energy of the accelerated ions. For removal of the SiO_xF_y passivation layer, same as for SiO_2 , an energy threshold around $10\text{--}30\ \text{eV}$ exists.⁷⁴ Lowering the RF power too much weakens the pursued ion bombardment to a degree, which may inhibit

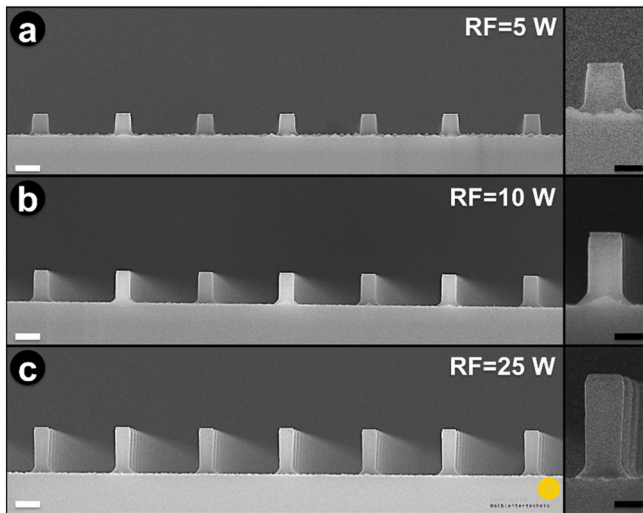


FIG. 19. Cross-sectional SEM graphs showing the influence of RF power on the fabrication of Si-NWAs using cryo-DRIE (recipe #Nano-Uniformity, 10 min, with the other process parameters fixed, process parameters; see Table I) and patterned nanodiscs of NIL resist ($D\sim 400\text{-P}\sim 3200\text{-H}\sim 600$) as masks, (a) RF power at 5 W, (b) RF power at 10 W, and (c) RF power at 25 W. Magnified views of corresponding single NWs are displayed on the right. The scale bars (white/black) correspond to $1\ \mu\text{m}/500\ \text{nm}$. The resist masks were removed after etching of the Si-NWAs.

directional etching of the SiO_xF_y layer leading to a rough surface and ending up with black-Si evolution. As it can be seen clearly in Fig. 19(c), higher RF power leads to less undercut than lower RF power [Figs. 19(a) and 19(b)], but more negatively profile, when using the same mask material. At higher RF power levels, because of the strengthened and more directional physical bombardment by the ions, the vertical etching rate of Si increases, while the lateral etching rate of Si underneath the masks is not appreciably affected. Meanwhile, higher ion energy results in more re-deposition of ions and radicals onto the NWs sidewalls, enhancing sidewall etching and forming a negative sidewall profile. In addition, higher ion energy results in lateral shrinkage of the mask discs due to more severe erosion, especially of resist masks, forming bowling-pin-shaped NWs similar to those found at increased etching temperatures.

5. Pressure

The helium pressure controls the heat transfer between the bottom electrode and the wafer carrier of stainless steel to ensure a sufficiently good thermal conductivity for efficient temperature transfer from the LN_2 cooling head to the silicon wafer and removal of the heat induced on the wafer by the plasma process.^{58,75–78} As the chamber pressure was reduced to 0.1 Pa [Fig. 20(a)], a minor mask undercut is observed at the start of the process followed by early removal of the sidewall passivation layer causing lateral etching by fluorine radicals. Consequently, the NW profiles have a negative sidewall angle. By applying a higher process pressure of 2.0 Pa [Fig. 20(c)], the ion bombardment has a larger ion angular distribution (IAD), which reduces the ion-bombardment directionality.⁵¹ The Si etch rate increases with pressure in the low-pressure region due to an increase in atomic

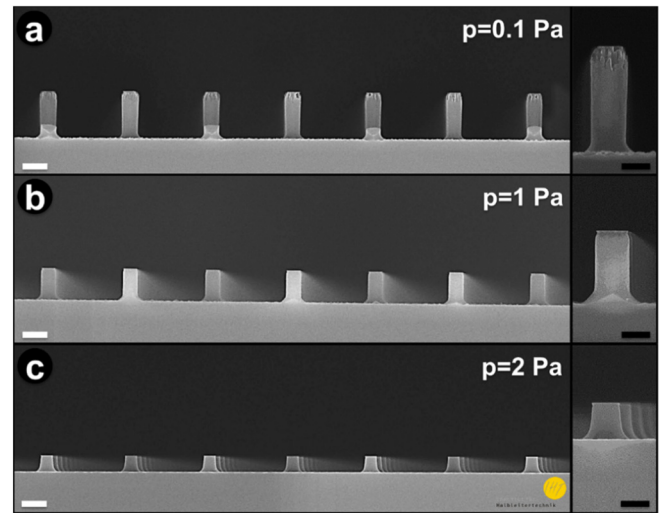


FIG. 20. Cross-sectional SEM graphs showing the influence of pressure on the fabrication of Si-NWAs using cryo-DRIE (recipe #Nano-Uniformity, 10 min, with the other process parameters fixed, process parameters; see Table I) and patterned nanodiscs of NIL resist ($D\sim 400\text{-P}\sim 3200\text{-H}\sim 600$) as masks, (a) chamber pressure at 0.1 Pa, (b) chamber pressure at 1 Pa, and (c) chamber pressure at 2 Pa. Magnified views of corresponding single NWs are displayed on the right. The scale bars (white/black) correspond to $1\ \mu\text{m}/500\ \text{nm}$. The resist masks were removed after etching of the Si-NWAs.

fluorine concentration. However, increasing pressure further results in a decreased etch rate due to decreased ion energy and radical flux in a high-pressure plasma. As a result, the fabrication of Si-NW is affected by the emergence of black Si (Fig. S18). Finally, it has been recognized that high-aspect-ratio etching of Si requires a sufficient (i.e., relatively high) flux of the process gases. Otherwise, a decrease in etch rate due to etch-species depletion was observed, which might lead to an overpassivation of the Si bottom surface causing an immediate stop of the etch process. Therefore, a maximum etch rate for fabricating HAR Si-NWAs of regular profile and smooth surface can be observed at a pressure between 0.1 and 1 Pa.

In addition, as observed in figures of all Si-NWAs etched from Si $\langle 100 \rangle$ and presented in this work, the cylindrical wire shape at the top goes into a square/cubic-shaped pedestal, indicating the low etch rate of the $\langle 111 \rangle$ planes. One rational explanation is the faster passivation rate on Si $\langle 111 \rangle$, since there is only a single dangling bond available from the Si atoms of the surface, which has to be saturated. This facilitated passivation of the crystal planes, which have higher densities is known from oxidation rates, i.e., oxidation of Si $\langle 111 \rangle$ is faster than Si $\langle 100 \rangle$.⁷⁹ McFeely *et al.* explained the different etch rates from an etching mechanism, in which at room temperature the silicon surface is covered by many monolayer thick SiF_2 films.⁸⁰ On Si $\langle 100 \rangle$, more SiF_2 species tend to evolve compared to Si $\langle 111 \rangle$. SiF_2 is considered to be the essential intermediate etching species to form the SiF_4 end product. For etching of Si $\langle 111 \rangle$ via the SiF_2 intermediate state, a Si-Si bond has to be broken, with an inherently higher activation energy and thus a lower etching rate on Si $\langle 111 \rangle$ than on Si $\langle 100 \rangle$. This state seems to be similar to the etching reactions of Si in wet HO-containing solutions.

In summary, the impact of individual cryo-DRIE parameters—namely, (a) temperature, (b) ICP power, (c) RF power, and (d) chamber

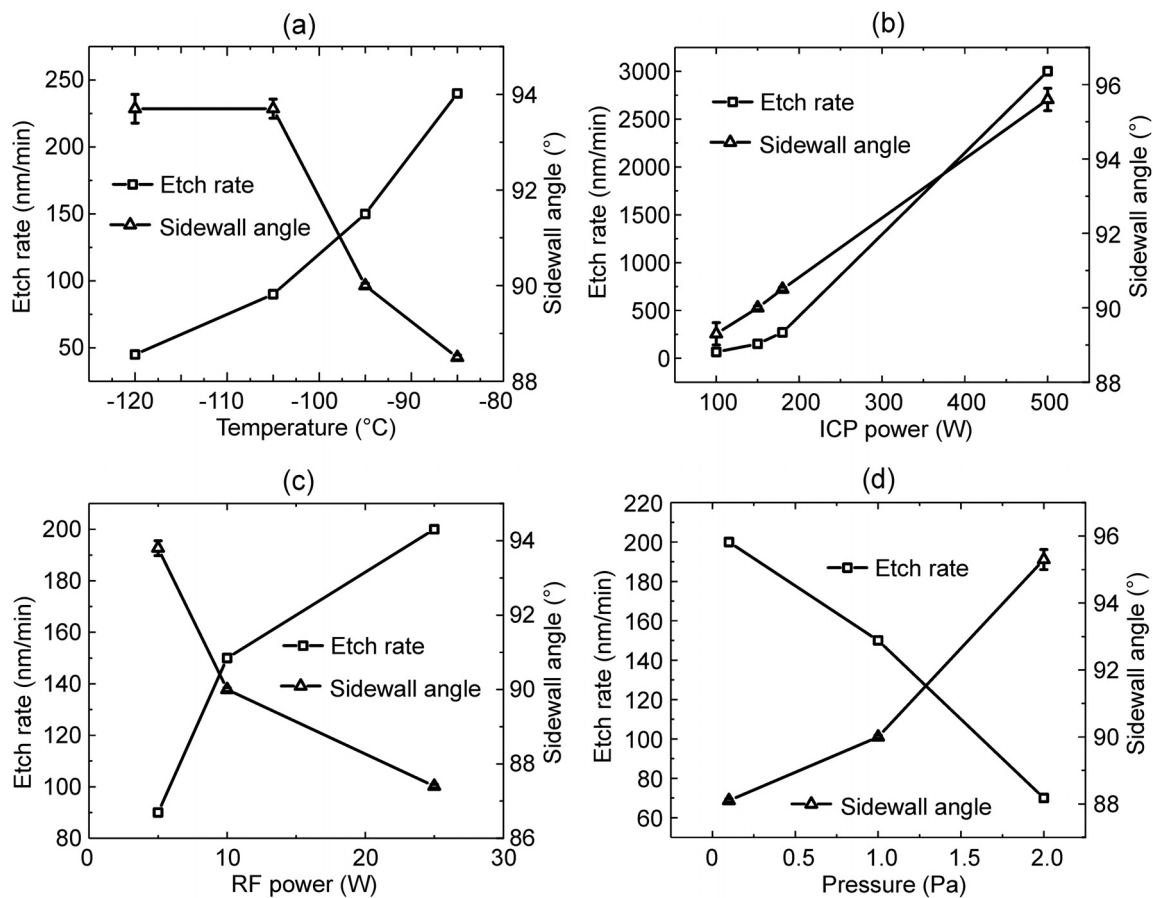


FIG. 21. Effect of the cryo-DRIE processing parameters on the etch rate and sidewall angle (sidewall inclination to the wafer bottom surface) of Si-NWAs, i.e. temperature (a), ICP power (b), RF power (c), and chamber pressure (d). The Si-NWAs were fabricated using (recipe #Nano-Uniformity, 10 min, Table I) with changes in the parameter given in each figure (a)–(d), using resists-nanodiscs (D~400-P~3200-H~600) patterned by NIL on Si (100) (phosphorus-doped, 1–10 $\Omega \times \text{cm}$, 4").

pressure—on the geometry and morphology of Si-NWAs has been illustrated in Fig. 21 (depicting etch rate and sidewall angle) and Fig. S19 (depicting height, diameter, and aspect ratio). As demonstrated in Sec. II C 1, a gas flux exceeding 60 sccm provides sufficient radicals for the etching reaction; therefore, etch rate will not be improved with increased gas flux further. Elevated etch rates can be achieved by enhancing ion density and ion activity, accomplished through increased ICP power and RF power, as well as maintaining higher chamber reaction temperatures or lower reaction pressures. For etching HAR Si-NWAs with a high etch rate, the optimal process involves using high ICP power (e.g., 500 W). The profile angle of Si-NWAs, influencing their macro physical properties and optical applications, is determined by the passivation rate of the reaction. Elevated temperature and pressure lead to increased passivation, resulting in positive profiles and cessation of etching until the formation of black silicon. Additionally, since RF power enhances physical etching, a low RF power is preferred during the initial stages of etching to reduce undercut, particularly when ion density is high. Excessively low RF power may lead to a positive profile, forming a thick passivation layer and hindering the formation of HAR Si-NWAs. To achieve extremely high-aspect-ratio (>100) Si-NWAs, RF power can be adjusted higher after the formation of HAR

Si-NWAs for a second cycle of etching, similar to the etching cycles in a conventional process. The effect of cryo-DRIE process parameters on topographical profiles exhibits dependencies that guide the optimization of a set recipe based on specific design requirements (aspect ratio, area density, diameter, surface roughness) and the characteristics of the utilized lithography techniques (PL, NSL, NIL, EBL).

D. EBL-doping dependence

By etching and comparing heavily doped ($\sim 10^{19} \text{ cm}^{-3}$) and lightly doped ($\sim 10^{12} \text{ cm}^{-3}$) Si wafers, it has been found that charge dissipation into substrates plays a negligible role in plasma etching and the wafer conductivity of Si is not important for mask undercut.³⁸ Here, various Si-NWAs are fabricated by etching different thick layers of intrinsic Si materials, which have been epitaxially grown on boron-doped Si (100) wafers with a dopant concentration of $\sim 2 \times 10^{19}$, phosphorus-doped Si (100) wafers with a dopant concentration of $\sim 7 \times 10^{18} \text{ cm}^{-3}$, arsenic-doped Si (111) wafers with a dopant concentration of $\sim 4 \times 10^{19} \text{ cm}^{-3}$ (see Ref. 81), as well as commercial four-inch wafers of phosphorus-doped Si (100) with a dopant concentration of $\sim 5 \times 10^{15} \text{ cm}^{-3}$ (SIEGERT WAFER, Germany), and boron-doped Si (111) wafers with

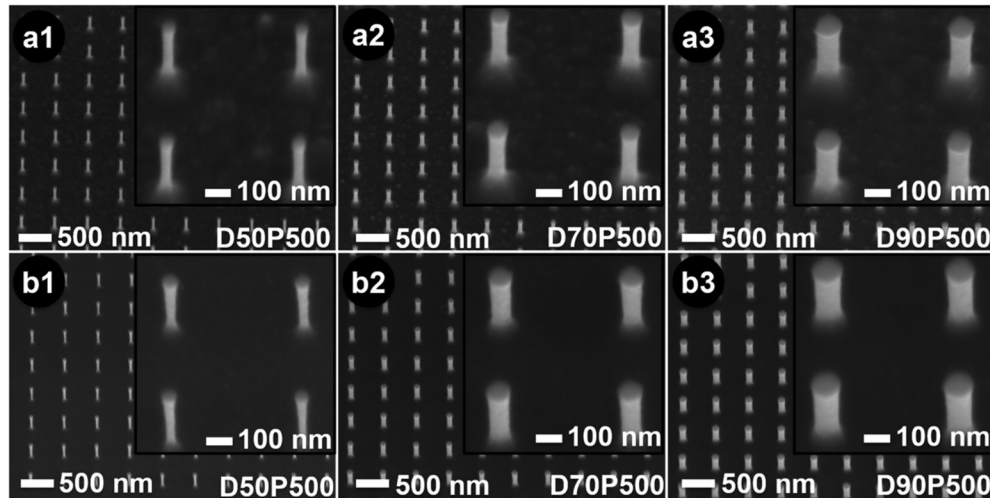


FIG. 22. 30° tilted-SEM graphs of Si-NWAs of different layouts (1) $d_m \approx 50$ nm, pitch ≈ 500 nm, (2) $d_m \approx 70$ nm, pitch ≈ 500 nm, and (3) $d_m \approx 90$ nm, pitch ≈ 500 nm, fabricated by cryo-DRIE (recipe: #sub-100 nm-2, 6 min, Table I) using EBL-patterned nanodisks of Cr (30 nm in thickness) as masks on 1×1 cm² Si with an intrinsic Si epitaxy layer on (a) phosphorus-doped Si $\langle 100 \rangle$ with a dopant concentration of $\sim 7 \times 10^{18}$ cm⁻³, and (b) arsenic-doped Si $\langle 111 \rangle$ with a dopant concentration of $\sim 4 \times 10^{19}$ cm⁻³. Insets are their corresponding magnified views (with Cr masks still on their top surfaces). The scale bars are 500 and 100 nm for the figures and their insets, respectively.

a dopant concentration of $\sim 8 \times 10^{13}$ cm⁻³. The diameters of fabricated Si-NWAs range from 30 to 1500 nm, cf. Figs. 22 and Fig. S5. An influence of the dopant type on cryo-DRIE has not been observed; however, crystal orientation is crucial to NW morphology, since Si $\langle 100 \rangle$ showed a rougher bottom surface finish after etching compared to Si $\langle 111 \rangle$. In addition, although n -Si $\langle 100 \rangle$ and p -Si $\langle 100 \rangle$ have visually identical morphology, the etch rate on n -Si $\langle 100 \rangle$ (~ 90 nm/min) is higher than on p -Si $\langle 100 \rangle$ (~ 78 nm/min) and n -Si $\langle 111 \rangle$ (~ 76 nm/min). This demonstrates that etch rate is dependent on doping type and crystallographic orientation.

As we see from Fig. 23, the Si-NWs have cylindrical shape with two sections of different diameters. The thicker upper cylinders (~ 1250 nm in height) are etched from a ~ 1250 -nm-thick epitaxial layer of intrinsic Si while the thinner lower cylinders originate from the highly doped n -Si $\langle 100 \rangle$ substrate. Since they have been etched at constant cryo-DRIE parameters (recipe: #sub-100 nm-2, 20 min, Table I),

we can conclude that the lateral etch rate of highly doped n -Si $\langle 100 \rangle$ is much higher than that of intrinsic Si. These results agree to a “charge transfer mechanism” (see Ref. 82), in which electron transfer from Si to physisorbed fluorine atoms is considered. The electron-transfer rate determines the chemisorption rate of fluorine atoms on the Si surface, which in turn controls the Si etch rate. Since highly phosphorous-doped n -Si has negatively charged surface states acting as electron donors, more electrons are offered. Exposed to neutral fluorine atoms, n -type Si can therefore accelerate F chemisorption, whereafter etch reactions will be notably promoted. Conversely, in p -type Si, positively charged surface states are expected acting as electron acceptors. In this case, for chemisorption of F, the electrons have to move from the fluorine atom to the surface state, which is unlikely because of the strong electronegativity of F.

To enhance the aspect ratio of the resulting Si-NWAs or further reduce the diameter of the NWs beyond the limits of nanolithography

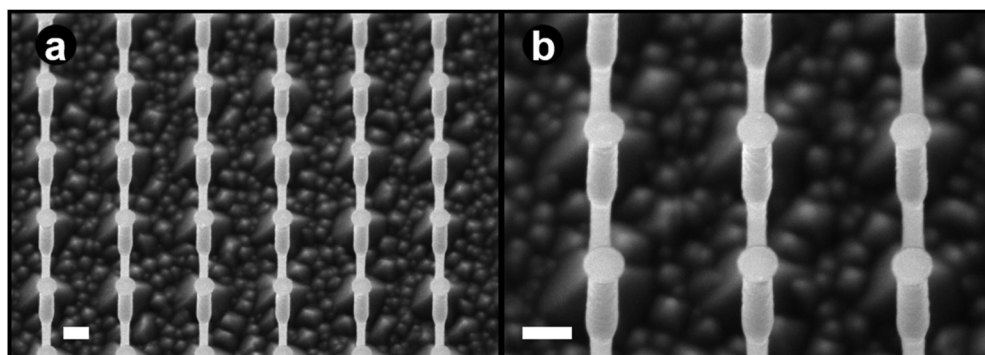


FIG. 23. (a) 30° tilted-SEM graphs of Si-NWAs fabricated by cryo-DRIE (recipe: #sub-100 nm-2, 20 min, Table I) using EBL-patterned nanodisks of Cr (D400P1500H30) as masks on 1×1 cm² Si with an intrinsic epitaxial layer on a phosphorus-doped Si $\langle 100 \rangle$ substrate with a dopant concentration of $\sim 7 \times 10^{18}$ cm⁻³, and its magnified view (b). The Si-NWAs are with Cr mask disks still on their tops. The scale bars are 500 nm.

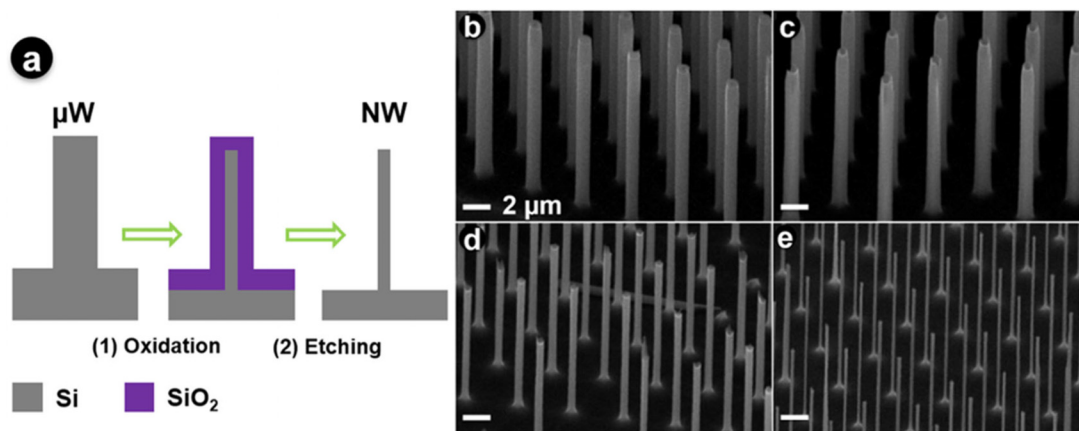


FIG. 24. Si-NWAs fabricated by cryo-DRIE (recipe #PL-HAR, $t = 5$ min, Table I), with patterned nanodiscs of photoresist AZ5214E ($D \sim 1200$ -P4000-H ~ 200) as masks, and their diameter reduction using thermal oxidation and wet-chemical etching. (a) Schematic of the NWs oxidation (1) and oxide-etching (2) process. (b) Si-NWAs fabricated by cryo-DRIE, (c), (d), and (e) showing SEM graphs of Si-NWAs after one, two and three cycles of oxidation and wet-chemical etching, respectively. The scale bars of (b)–(e) are $2 \mu\text{m}$.

techniques, a post-etching oxidation (POE) and oxide-stripping process can be employed [Fig. 24(a)]. In our investigation, Si-NWs obtained through cryo-DRIE using a PL-mask undergo initial thermal oxidation at 1100°C .^{83,84} Subsequently, the formed Si oxide layer is eliminated by immersing the Si-NWA sample in a diluted HF solution (6%–7%). As depicted in Figs. 24(b)–24(e) and Fig. S20 in the supplementary material (SI), the diameters of Si-NWs can be linearly reduced from approximately 1060 nm to around 230 nm over three cycles. However, the thinning of NWs through POE/oxide-stripping is time-intensive and limited to producing Si-NWAs with pitches larger than the micrometer range. Additionally, achieving uniform oxidation/oxide-etching necessitates precise experimental conditions, as deviations can lead to deflection or collapse of Si-NWs (diameter ~ 200 nm, aspect ratio of ~ 90 , Fig. S21), similar to challenges encountered in the wet-MacEtch process due to liquid drying.

The pattern collapses of vertically standing high-aspect-ratio NWs due to stiction, which are well-known for wet-MacEtch, can be circumvented using “dry” etching methods like gas-MacEtch, the Bosch process, the pseudo-Bosch process, and the cryo-DRIE. These techniques are therefore preferred for fabricating highly ordered Si-NWs on large-scale areas. In the case of extremely high aspect ratios, the reactant gases need to diffuse through the already etched NWs to reach the bottom surface (or a catalyst at the bottom surface for the gas-MacEtch). With continued etching, the process is becoming more and more diffusion limited. In gas-MacEtch, however, the used catalyst film patterns start to deform and to initiate a spiraling catalyst motion inside the Si substrate, as described in Ref. 35. Such an effect is absent in plasma enhanced dry etching (cryo-DRIE and the pseudo-Bosch), in which RF power can be tuned to proceed the etching toward high-aspect-ratio NWs. As summarized in Table IV, cryo-DRIE technique offers distinct advantages in the fabrication of Si-NWAs compared to the conventional Bosch and pseudo-Bosch processes. Cryo-DRIE enables the realization of Si-NWAs with greater heights and aspect ratios. Furthermore, through optimization of etching recipes or the implementation of switching cryo-DRIE techniques, it becomes feasible to fabricate Si-NWAs with heights equivalent to those

achieved by gas-MacEtch. Notably, cryo-DRIE exhibits unique advantages in etching sub-100-nm diameter Si-NWAs, such as a high mask dimension spatial transfer and low roughness surface, which are unattainable using alternative techniques. This highlights the potential of cryo-DRIE for fabricating and processing nanostructures and devices of extremely small dimensions.

In addition to its technical advantages, cryo-DRIE offers notable cleanliness compared to the pseudo-Bosch process and gas-MacEtch. The latter two techniques require the subsequent removal of passivation layers or noble-metal catalyst layers, respectively, which pose challenges for Si doping in electronics applications. The presence of these layers necessitates additional steps for their removal, including wet-chemical etching, which compromises the stiction-free processing advantage offered by dry etching techniques thus far. Furthermore, cryo-DRIE exhibits a higher throughput, allowing for a greater number of wafers to be etched per hour. Its etch rate is comparable to the Bosch and pseudo-Bosch processes, significantly higher than that of gas-MacEtch. Moreover, cryo-DRIE eliminates the need for an additional passivation layer cleaning step. Overall, cryo-DRIE presents a promising avenue for the fabrication of Si-NWAs, offering superior control over dimensions, cleanliness, and throughput compared to alternative techniques.

III. CONCLUSION

In this study, we have shown that anisotropic deep-reactive ion etching of silicon at cryogenic temperatures (cryo-DRIE) has good capability and potential for fabricating high-aspect-ratio sub- μm and further sub-100-nm vertical arrays of silicon nanowires (Si-NWs). Through our optimized etching process parameters, we have shown that Si-NWs as small as ~ 10 nm in diameter and large-scale silicon nanowire arrays (Si-NWAs) as small as ~ 30 nm in diameter can be realized. Furthermore, for high-aspect-ratio Si-NWs by cryo-DRIE, we achieved selectivity of $\sim 100:1$ with UV photoresist (AZ5214), of $> 120:1$ with UV nanoimprint resist and $> 667:1$ with a Cr hard mask, which are much higher than those reported for the Bosch or pseudo-Bosch process. In addition, cryo-DRIE enables us to

manufacture Si-NWs of large heights of more than $20\ \mu\text{m}$ (aspect ratio > 100) and low sidewall roughness ($13\ \text{nm}$) without scalloping, with high etch rates of $> 4\ \mu\text{m}/\text{min}$, comparable to the Bosch process, and much higher than those provided by pseudo-Bosch and gas-phase metal-assisted chemical etching (gas-MacEtch), and smooth surface finish (top roughness $\sim 0.3\ \text{nm}$, bottom-space roughness $\sim 2\ \text{nm}$). In addition, compared to the Bosch process and pseudo-Bosch process, the cryo-DRIE has less undercut; therefore, mask patterns can be better transferred to nanostructures with less dimension deviation, which is beneficial for fabricating nanodevices with precise high-resolution demands. Additionally, ion irradiation at lower kinetic energy, given by radio frequency (RF) power, can be used in the cryo-DRIE process, which produces less damage to the nanostructures.

Furthermore, the number of etched wafers per hours can be higher using cryo-DRIE, since it is a clean wafer-scale etching process. Different to the Bosch process and pseudo-Bosch process, neither the sample nor the reaction chamber has to be cleaned after cryo-DRIE to remove the passivation layer. Compared to the gas-MacEtch, which requires removing a noble-metal catalyst layer from the bottom between the NWs, the masks for cryo-DRIE can be easily removed from the top of Si-NWs by either dry- or wet-chemical etching. Furthermore, cryo-DRIE offers much higher etch rates than gas-MacEtch. Furthermore, cryo-DRIE presents a promising avenue for the manufacturing of periodic nanoscale 3D Si architectures, exploiting UV and EBL resists for patterning transfer without using hard masks, which offer significant benefits for industrial production in emerging fields such as next-generation photonics and electronics.

Comprehensive dimensional and topographical metrology of Si-NWAs was done using different methods including high-resolution imaging of individual NWs within a micrometer-scale field of view using AFM and SEM and collective inspection of arrays on millimeter scale using optical scatterometry (angle-resolved Mueller matrix polarimetry, angle-resolved Fourier microscopy). As prerequisite for metrology during high-volume manufacturing of Si-NWAs at high throughput, methods may be combined into a hybrid metrology, where the strength of a specific method is used to compensate for the weakness of another and vice versa. NW height accurately determined with sub-nanometer resolution on few NWs can be used as an a-priori known input parameter for optical scatterometry providing a sub-nanometer uncertainty of diameter determined with $> 10^5$ NWs over a nearly millimeter-scale field of view. Imaging at varied magnification for selecting a specific NW from an array was combined with traceable roughness measurement on its top and sidewall surfaces using SEM and AFM in one system.

IV. METHODS

A. Mask materials and fabrication techniques

Ideal NWs can be fabricated only under the premise of choosing advisable patterning technologies for preparing appropriate lithography masks, according to the corresponding etching techniques and semiconductor substrates. For example, to Si-NWAs, masks of patterned nanodisc arrays or nanohole arrays are required for dry etching and MacEtch, respectively. Mask materials are generally categorized into two types: soft masks and hard masks. Soft masks are usually resist-structures patterned by a lithography process. As the mainstay of micro- and nanoscale processing, a semiconductor lithography system undertakes the fabrication of mask patterns. It is, therefore,

determinative and crucial to push dimensional limits of nanostructures further before studying the effects of process parameters yielding NWs.

Selection of mask materials for etching is a critical issue, which may affect etch rate, mask undercutting, and surface quality of etched NWs. In addition, the patterning and preparation of adopted masks should be easy, and their resistance against etching must be sufficient. The combination of a suitable mask material and an appropriate anisotropic etching process is essential to fabricate Si-NWAs with expected dimensions (diameters and heights, etc.) and morphology (profile and smoothness of sidewalls, etc.). In cryo-DRIE, the major malady of photoresist masks in addition to resolution limits is their vulnerability to cracking due to thermal-expansion-mismatch stresses. Thin photoresists ($< 1.5\ \mu\text{m}$) are reported to be free of cracking problems but may limit the aspect ratio of NWs due to limited resistance against etching.⁵⁴ Compared to resists or polymers, which have limited etching resistance, hard masks are required for prolonged etching, which, again, are known to be sturdy to cracking at cryogenic temperatures. Aluminum has extremely high selectivity against Si in fluorine-based plasmas during cryo-DRIE, but it initiates the formation of Si “grass” on the bottom surface between the wires; therefore, its application as mask material is limited mainly to through-wafer-vias (TSVs) etching rather than employed for high-aspect-ratio nanostructures.⁸⁵ Jansen *et al.* reported that using SF_6 plus a passivation gas (O_2 , CHF_3 , or C_4F_8) at $0\ ^\circ\text{C}$ to $-120\ ^\circ\text{C}$, Cr masks will give more lateral etching than SiO_2 masks for both mixed-mode (i.e., non-switching) and pulsed-mode (i.e., switching) etching.⁸⁶

Photolithography (PL, also called optical lithography or UV lithography) is a well-known and well-established technique for realizing micro- and nanopatterns on silicon. It uses UV light to transfer a geometric pattern from a photomask to a photoresistive film on the substrate, which is homogeneously spin- or spray-coated over the entire substrate. Due to its advantages such as a large number of optional resist types and fast wafer-level processing, conventional PL has been the mostly employed technique for processing Si materials.^{87–89} Both masks of photoresist and metal can be fabricated by photolithography (Fig. 1). When preparing photoresist-based patterns on a Si substrate [Fig. 1(a)] for NWs etching, a mask with either a micro-/nanodisc array (for positive resist exposure) or a micro-/nanohole array (for negative resist exposure) is used, realizing patterns of micro-/nanodiscs [Fig. 1(b)] after developing, which works as mask for the subsequent etching. On the contrary, for the fabrication of metal masks, prior to the metal deposition, a “negative” pattern instead of the above-mentioned mask layout [Fig. 1(b*1)] has to be prepared. Hereafter, a metal (Cr, in our work) layer can be deposited forming circular micro-/nanodiscs as hard masks after a liftoff process [Fig. 1(b*2)]. In our experiments, both resist AZ5214 E (Microchemicals GmbH, Germany) and a $\sim 300\text{-nm}$ -thick Cr layer have been fabricated accordingly on Si wafers as etching masks. However, the traditional photolithography is inherently limited by the wavelength of the used light yielding a resolution typically not smaller than $400\ \text{nm}$.

Electron-beam lithography (known as e-beam lithography, EBL) can realize nanopatterns down to $\sim 2\ \text{nm}$ by exposing a polymeric thin resist film under a highly focused electron beam.⁹⁰ Generally, the EBL process contains steps similar to those applied during PL. Although low throughput is limiting the application of EBL in high-volume production of semiconductor devices, it has the primary advantage of

being a mask-less (direct-write) process. It generates defect-free and geometrically flexible nanopatterns, making it attractive for prototyping and specialized processing. The positive resist poly(methyl methacrylate) (PMMA, P 672.03 AR-P 672, Allresist GmbH, Germany), which is soluble after electron exposure due to chain breakage of long into smaller polymers, has been used in our research for creating nanoholes [Fig. 1(b*1)] as small as ~ 30 nm in diameter for Cr liftoff.⁹¹ For this work, a field-emission scanning electron microscope (FE-SEM, Supra 40, Carl Zeiss AG, Germany) was used. This FE-SEM is equipped with an e-beam writer (Raith, type EBPG 5200, 100 KeV, Raith GmbH, Germany) and can provide accurate exposure nominally down to ~ 10 nm. Cr with a thickness of 30 nm and diameters varying from 30 nm to 1500 nm have been fabricated as masks for etching experiments in this study.

Nanosphere lithography (NSL) or colloidal lithography (CL) has been extensively investigated in combination with MacEtch for fabricating Si-NWAs, due to its simplicity, low cost, and high throughput for constructing uniform nanopatterns compared to conventional nanolithography methods.^{92–96} In an NSL process, periodic arrays of self-assembled closed-packed mono/bilayer nanospheres [e.g., polystyrene (PS), SiO₂, and others] serve as masks. Polystyrene nanoparticles (PS-NPs) of ~ 200 and ~ 500 nm in diameters have been employed as etching masks in our work (Fig. S2). The order and uniformity of PS-NPs' deposition areas have been promoted by PL mesh arrays.⁵⁵

UV-based nanoimprint lithography (UV-NIL) enables a feasible cost-efficient process with high throughput, in which a transparent mold was pressed against photo-curable resist at room temperature. For the fabrication of Si-NWs, in this report, a flexible mold was employed instead of the conventional hard mold; therefore, fabrication errors such as imprecision due to non-planar and rough surface can be compensated by a conformal contact between the flexible mold and the Si substrate.^{56,97–102} Nanopatterned resists of UV Cur06 (Microresist technology GmbH, Germany) with lateral sizes ranging from 400 nm to 2 μ m with sequential increase in the pitch value from 800 nm to 4 μ m, and with a fixed lateral size of 200 nm and pitch of 500 nm have been utilized for etching Si-NWAs, details about the fabrication parameters and steps can be found elsewhere.^{56,103} Details on masks of various sizes and different materials that have been fabricated and used in this work, including mask parameters and fabrication techniques, have been summarized as Table V.

B. Si substrates and cryo-DRIE processing recipes

In a cryo-DRIE system, ICP and RF power are set individually to control ions/radicals flux and ion energy independently, with quite high power supplied to the ICP source to create a high-density plasma and a high density of etching species. For a defined kinetic energy of

the ions, the sample is biased by an RF power. The sample is placed on a substrate holder situated in the lower part of the reactor, on a chuck, which is cooled with liquid nitrogen. Its temperature is measured and regulated by a proportional-integral-derivative (PID) controlled heating element, which allows the wafer temperature to be set to a desired value. Helium is injected between the substrate and the chuck to increase thermal conductivity and facilitate the dissipation of heat generated from both the plasma and the chemical reactions. Therefore, to achieve “perfect Si-NWAs,” how do these aforementioned parameters (ICP power, RF power, temperature, pressure, etc.) influence the cryo-DRIE process, especially in the nanoscales, has to be experimentally characterized and understood, and subsequently optimized according to the designed mask layouts.

Experiments have been carried out in two cryo-DRIE systems (ICP-RIE plasma etcher SI 500, SENTECH, Germany, and PlasmaPro 100 RIE, Oxford Instruments, UK) by processing standard 2- to 4-inch silicon wafers of different orientations ($\langle 100 \rangle$ and $\langle 111 \rangle$). In addition, layers of intrinsic Si of different thicknesses, which have been epitaxially grown on highly B-doped and P-doped $\langle 100 \rangle$ substrates with dopant concentrations of 8×10^{19} and 7×10^{18} cm⁻³, respectively, have been etched as well. Because the etching process parameters were found to be compatible across the two ICP-RIE plasma etchers, we will not label the etching instruments distinctly in the description of the etching configuration in the paper. Prior to the cryo-DRIE process, all the samples/wafers have been immersed into 6% HF solution for 10–30 s to remove their native oxide layer.

C. Characterization of Si nanowires

1. Scanning electron microscopy for pitch measurement

Scanning electron microscopy (SEM) observation of uniformity and fidelity for the pitch and diameter was carried out on TESCAN MIRA's third-generation SEM (TESCAN ORSAY HOLDING, a.s. Czech Republic) at TU Braunschweig, Germany and an Ultra Plus (Zeiss) at the Laboratoire National de métrologie et d'Essais (LNE), Trappes, France. The latter is a Field Emission Gun (FEG) SEM equipped with a GEMINI column. The instrument was calibrated with P900H60 standard.¹⁰⁴ The main influencing parameters were set to 3–5 kV for the voltage (EHT) and 3.5–8 mm for the working distance (WD).

2. Angle-resolved Mueller matrix polarimeter (ARMMP)

In comparison with SEM and atomic force microscopy (AFM) techniques, optical metrology provides faster information about average feature dimensions at larger areas.¹⁰⁵ In the realm of critical dimensional characterization, spectral ellipsometry is widely employed

TABLE V. Masks adopted in this report for cryo-DRIE and their corresponding geometrical parameters. PS-NPs: Polystyrene nanoparticles.

Mask	Fabrication technique	Diameter (nm)	Pitch (nm)	Thickness (nm)
Resist, AZ5214E	UV-PL	1000	2400/4000	200/300
Cr	UV-NIL/PL	400/800	2400/3200	300
PS-NPs	NSL	200/500	$\sim 200/500$	$\sim 200/500$
Resist, UV Cur 06	UV-NIL	250/400/800	500/2400/3200/4000	300/600
Cr	EBL	30–1500	500–5000	30

to accurately determine the heights and diameters of periodic nanowire arrays (Si-NWAs). Although these techniques are commonly utilized, they primarily provide information on structure symmetry and surface orientations when the plane of incidence aligns with the principal directions of the silicon wafer. However, to gain insights into structure asymmetry and surface inclinations, it is advantageous to deviate from the standard configuration and rotate the plane of incidence. Traditionally, this involves rotating the sample and collecting data at multiple azimuthal angles, a laborious and infrequently used process. Alternatively, a rapid solution involves employing experimental setups featuring high numerical aperture microscope objectives to capture the Fourier plane image in a single acquisition. This innovative approach facilitates data collection for all incidence and azimuthal angles simultaneously, offering additional information crucial for determining the geometry of non-vertical walls.

In addition to other optical techniques, the Mueller matrix (MM) ellipsometry (Sec. IV C 2) can further obtain information about structure symmetry, which is directly related to the symmetry in the off-diagonal MM components. In the case of Fourier-space measurements of MM using objectives with high numerical aperture, the mixing of specular and diffracted light from periodic structures leads to an inevitable depolarization of the MMs in pixels where multiple orders overlap. This can be further analyzed as overlapping of diffraction orders in the case of non-coherent light sources, which leads directly to the sum of MMs corresponding to each separate diffraction order. While the analysis of such situation is more complex, it enables to access the information in multiple diffraction orders at the same time, thus allowing for a higher sensitivity to the structure parameters if all the data can be fully exploited (note that for another diffraction orders to appear, grating period has to be larger than the half of the wavelength of the probing light).

In order to further exploit a maximum of the available information, we have used an angle-resolved Mueller matrix polarimeter (ARMMP) to acquire complete MMs.¹⁰⁶ The setup operates thanks to eigenvalue calibration developed for a situation without explicit knowledge of the polarization properties of all components. Following this, calibration process enables to characterize all linear optical effects using the two calibration matrices A and W.¹⁰⁷ The setup is calibrated for every pixel taken by a CCD camera separately or in blocks of pixels.

3. Angle-resolved Fourier microscope (ARFM)

Angle-resolved Fourier microscopy (ARFM) measures the first element of the Mueller matrix (MM) that is not measured by angle-resolved MM ellipsometry. The setup collects data for all incidence and azimuthal angles simultaneously providing immediately the Fourier-space symmetry of periodic structures. We have done dimensional parameter retrieval from measured scatterometry efficiencies based on a recently developed hybrid metrology approach.^{72,108} As a result, angle-resolved Fourier microscopy showed a very high sensitivity to the diameter of periodically ordered vertical NWs, while sensitivity to their height is low. Hybrid metrology using height data measured beforehand by AFM as a-priori input for angle-resolved Fourier microscopy is therefore essential for obtaining dimensional parameters of vertical Si-NWAs on large scale with low uncertainties.

Hybrid metrology is used to determine the dimensional parameters and their uncertainties of 2D periodic NWs by measuring the same periodic structure using ARFM and AFM and applying a χ^2 -regression method with regularization that finds the best solution

based on the input from the two instruments.⁷² We have measured a square-patterned periodic with cylindrical shapes silicon NWs with a 500 nm pitch in the x and y directions, using ARFM and AFM. The χ^2 -regression method contains two parts, the first part includes the scatterometry contribution, while the second part is a Tikhonov regularization part¹⁰⁸ used for including the height measured in advance using AFM. ARFM is an inverse technique that requires a rigorous Maxwell's solver to find the dimensions of a periodic structure.¹⁰⁹ The inverse problem we consider is the task of calculating from a set of measurements of the dimensional parameters that produced those results. The approach used here is based on setting up a regression problem in the following sense: given a vector y of the measurement data space R_n ($y \in R_n$), a rigorous coupled-wave analysis (RCWA) model function, f_{RCWA} , maps a dimensional parameter p , which we want to determine, to the measurement space R_m ($p \in R_m$, $f_{RCWA}: R_m \rightarrow R_n$). f_{RCWA} transforms the parameter p into calculated model scattering-diffraction efficiencies (η^c), resulting in an approximation to the measured data y . If additional knowledge about the measurement errors is available, e.g., if the variances σ_i^2 of each of the measured values y_i are known, one can give them a corresponding weight in the regression procedure. Then, the hybrid χ^2 function based on the input from ARFM and AFM is written as⁷²

$$\chi^2(p^c) = \frac{1}{2} \left(\frac{(h - h^c)^2}{(\sigma_{AFM})^2} + \frac{1}{N} \sum_{i=1}^N \frac{(\eta - \eta^c(i, p^c))^2}{(\sigma_{\eta}(i))^2} \right). \quad (2)$$

Here, the superscript c indicates calculated parameters, p^c is a shorthand notation for all the calculated geometrical parameters in the mathematical model, σ_{AFM} is the uncertainty of NW height h measured by AFM, and $\sigma_{\eta}(i)$ is the uncertainty of the i th pixel ($i = 1, \dots, N$, $N = 121 \times 121$), measured by ARFM. The above equation is used to find best agreement of a library of pre-calculated Fourier scattering-diffraction efficiency images with the experiment. Then, we can estimate the corresponding uncertainties $u(p)$, from the diagonal elements of the covariance matrix (Σ) using

$$\Sigma = (J^T U J)^{-1}, \quad (3)$$

where U is a diagonal matrix containing all the squared measurements uncertainties and J is the Jacobian of η^c and h^c . For uncertainty analysis, we assume perfect microscope objective, lenses, and light alignment.

4. Roughness and height measurements of Si nanowires by atomic force microscopy (AFM)

Roughness and height of Si-NWs have been determined with LNE's commercial atomic force microscope (AFM), which is a Bruker Dimension 3100 with nanoman-V controller. It has been calibrated with a standard in the same range as the expected height values. Thus, the AFM was calibrated with a step height SHS B1000 standard provided by PTB. Its reference value was evaluated using LNE's metrological AFM.¹¹⁰

5. Roughness measurement of Si Nanowires by FusionScope™

Roughness measurements of sidewalls, top, and bottom-space surface of Si-NWs have been performed with a FusionScope™ (Quantum Design, San Diego, USA), an AFM, and an SEM combined in one system.¹¹¹ All AFM and SEM measurements in the FusionScope™ have

been performed under high vacuum conditions. SEM imaging has been performed with a beam accelerating voltage of 5 kV. Diamond tips glued on self-sensing cantilevers (AMG Technology Ltd., Botevgrad, Bulgaria) with piezo-resistive readout have been utilized. The resonance frequency of the cantilever ranges between 450 and 550 kHz and the spring constant between 12 and 330 N/m. All AFM measurements have been performed in the amplitude-modulation mode. For visualization, AFM data have been post-processed using the Gwyddion software (V2.60). Plane subtraction, three-point leveling, and line-by-line subtraction have been used.

SUPPLEMENTARY MATERIAL

See the supplementary material for the fabrication of colloidal mask, layout of masks fabricated by e-beam lithography, discussion of Si-NWs fabrication, influence of loading effects and aspect-ratio-dependent etching, and characterization of Si-NWAs.

ACKNOWLEDGMENTS

The project (19ENG05 NanoWires) has received funding from the EMPIR programme co-financed by the Participating States and from the European Union's Horizon 2020 research and innovation program. A. D. R. and E. P. acknowledge the funding support from the German Federal Ministry of Education and Research (BMBF) for the project "3D nano-engineered silicon anodes for high-energy-density lithium-ion rechargeable batteries (SiNanoBatt)" under no 01DP21003.

AUTHOR DECLARATIONS

Conflict of Interest

The authors have no conflicts to disclose.

Author Contributions

Jiushuai Xu: Conceptualization (lead); Data curation (lead); Formal analysis (equal); Investigation (lead); Methodology (lead); Validation (lead); Writing—original draft (lead); Writing—review & editing (lead). **Hutomo Suryo Wasisto:** Investigation (supporting); Validation (supporting); Writing—review & editing (supporting). **Jonathan Kottmeier:** Investigation (supporting); Methodology (supporting); Resources (equal); Writing—review & editing (supporting). **Andreas Dietzel:** Investigation (supporting); Methodology (supporting); Resources (equal). **Thomas Weimann:** Investigation (supporting); Methodology (supporting); Resources (equal); Validation (equal); Writing—review & editing (equal). **Jan K. Prüßing:** Investigation (supporting); Methodology (supporting); Resources (equal); Validation (equal); Writing—review & editing (supporting). **Hartmut A. Bracht:** Investigation (supporting); Methodology (supporting); Resources (equal); Validation (equal); Writing—review & editing (supporting). **Erwin Peiner:** Conceptualization (equal); Funding acquisition (lead); Investigation (supporting); Methodology (equal); Project administration (lead); Resources (equal); Supervision (lead); Validation (equal); Writing—original draft (supporting); Writing—review & editing (equal). **Andam Deatama Refino:** Data curation (supporting); Investigation (supporting); Writing—review & editing (supporting). **Alexandra Delvallée:** Conceptualization (supporting); Data curation (equal); Investigation (supporting); Methodology (equal); Validation (equal); Writing—original draft (supporting);

Writing—review & editing (equal). **Sebastian Seibert:** Data curation (equal); Investigation (supporting); Methodology (equal); Validation (equal); Visualization (equal); Writing—original draft (supporting); Writing—review & editing (supporting). **Christian Schwalb:** Conceptualization (supporting); Data curation (equal); Investigation (supporting); Methodology (equal); Resources (equal); Validation (equal); Writing—original draft (supporting); Writing—review & editing (supporting). **Poul Erik Hansen:** Investigation (equal); Methodology (equal); Software (equal); Writing—original draft (equal); Writing—review & editing (equal). **Martin Foldyna:** Conceptualization (supporting); Data curation (equal); Investigation (supporting); Methodology (equal); Validation (equal); Visualization (equal); Writing—original draft (supporting); Writing—review & editing (equal). **Lauryna Siaudyte:** Investigation (supporting); Methodology (supporting); Resources (supporting); Software (supporting); Writing—review & editing (supporting). **Gerry Hamdana:** Conceptualization (supporting); Data curation (supporting); Investigation (supporting); Methodology (supporting); Validation (supporting); Writing—review & editing (supporting).

DATA AVAILABILITY

The data that support the findings of this study are available from the corresponding author upon reasonable request.

REFERENCES

- ¹S. Raman, A. Ravi Sankar, and M. Sindhuja, "Advances in silicon nanowire applications in energy generation, storage, sensing, and electronics: A review," *Nanotechnology* **34**(18), 182001 (2023).
- ²A. D. Refino, N. Yulianto, I. Syamsu, A. P. Nugroho, N. H. Hawari, A. Syring, E. Kartini, F. Iskandar, T. Voss, A. Sumboja, E. Peiner, and H. S. Wasisto, "Versatilely tuned vertical silicon nanowire arrays by cryogenic reactive ion etching as a lithium-ion battery anode," *Sci Rep.* **11**(1), 19779 (2021).
- ³C. A. Dirdal, K. Milenko, A. Summanwar, F. T. Dullo, P. C. V. Thrane, O. Rasoga, A. M. Avram, A. Dinescu, and A. M. Baracu, "UV-nanoimprint and deep reactive ion etching of high efficiency silicon metalenses: High throughput at low cost with excellent resolution and repeatability," *Nanomaterials* **13**(3), 436 (2023).
- ⁴Y. Cui, Z. Zhong, D. Wang, W. U. Wang, and C. M. Lieber, "High performance silicon nanowire field effect transistors," *Nano Lett.* **3**(2), 149–152 (2003).
- ⁵S. Rahong, T. Yasui, N. Kaji, and Y. Baba, "Recent developments in nanowires for bio-applications from molecular to cellular levels," *Lab Chip* **16**(7), 1126–1138 (2016).
- ⁶A. Stranz, A. Waag, and E. Peiner, "High-temperature performance of stacked silicon nanowires for thermoelectric power generation," *J. Electron. Mater.* **42**(7), 2233–2238 (2013).
- ⁷S. Lee, K. Kim, D. H. Kang, M. Meyyappan, and C. K. Baek, "Vertical silicon nanowire thermoelectric modules with enhanced thermoelectric properties," *Nano Lett.* **19**(2), 747–755 (2019).
- ⁸Y. Li, M. Li, R. Li, P. Fu, B. Jiang, D. Song, C. Shen, Y. Zhao, and R. Huang, "Linear length-dependent light-harvesting ability of silicon nanowire," *Opt. Commun.* **355**, 6–9 (2015).
- ⁹W. Jevasuwan, J. Chen, T. Subramani, K. C. Pradel, T. Takei, K. Dai, K. Shinotsuka, Y. Hatta, and N. Fukata, "Pencil-shaped silicon nanowire synthesis and photovoltaic application," *Jpn. J. Appl. Phys.* **56**(8), 085201 (2017).
- ¹⁰J. Soueiri, R. Saredidine, H. Kadiri, A. Alhussein, G. Lerondel, and R. Habchi, "A review of cost-effective black silicon fabrication techniques and applications," *Nanoscale* **15**(10), 4738–4761 (2023).
- ¹¹P. G. Maloney, P. Smith, V. King, C. Billman, M. Winkler, and E. Mazur, "Emissivity of microstructured silicon," *Appl. Opt.* **49**(7), 1065–1068 (2010).

- ¹²Y. Liu, S. Liu, Y. Wang, G. Feng, J. Zhu, and L. Zhao, "Broad band enhanced infrared light absorption of a femtosecond laser microstructured silicon," *Laser Phys.* **18**(10), 1148–1152 (2008).
- ¹³S. Sarkar, A. A. Elsayed, Y. M. Sabry, F. Marty, J. Drévilion, X. Liu, Z. Liang, E. Richalot, P. Basset, E. Nefzaoui, and T. Bourouina, "Black silicon revisited as an ultrabroadband perfect infrared absorber over 20 μm wavelength range," *Adv. Photonics Res.* **4**(2), 2200223 (2023).
- ¹⁴A. P. Nugroho, N. H. Hawari, B. Prakoso, A. D. Refino, N. Yulianto, F. Iskandar, E. Kartini, E. Peiner, H. S. Wasisto, and A. Sumboja, "Vertically aligned n-type silicon nanowire array as a free-standing anode for lithium-ion batteries," *Nanomaterials* **11**(11), 3137 (2021).
- ¹⁵S. M. Thalluri, J. Borme, D. Xiong, J. Xu, W. Li, I. Amorim, P. Alpuim, J. Gaspar, H. Fonseca, L. Qiao, and L. Liu, "Highly-ordered silicon nanowire arrays for photoelectrochemical hydrogen evolution: An investigation on the effect of wire diameter, length and inter-wire spacing," *Sustain Energy Fuels* **2**(5), 978–982 (2018).
- ¹⁶Z. Zhang, Y. Wang, P. A. Stensby Hansen, K. Du, K. R. Gustavsen, G. Liu, F. Karlsen, O. Nilsen, C. Xue, and K. Wang, "Black silicon with order-disordered structures for enhanced light trapping and photothermal conversion," *Nano Energy* **65**, 103992 (2019).
- ¹⁷C. Hwang, K. Lee, H.-D. Um, Y. Lee, K. Seo, and H.-K. Song, "Conductive and porous silicon nanowire anodes for lithium ion batteries," *J. Electrochem. Soc.* **164**(7), A1564–A1568 (2017).
- ¹⁸S. Gopalakrishnan and K. Jegannathan, "Facile fabrication of silicon nanowires as photocathode for visible-light induced photoelectrochemical water splitting," *Int. J. Hydrogen Energy* **42**(36), 22671–22676 (2017).
- ¹⁹S. A. Fortuna and X. Li, "Metal-catalyzed semiconductor nanowires: A review on the control of growth directions," *Semicond. Sci. Technol.* **25**(2), 024005 (2010).
- ²⁰S. W. Chang, V. P. Chuang, S. T. Boles, C. A. Ross, and C. V. Thompson, "Densely packed arrays of ultra-high-aspect-ratio silicon nanowires fabricated using block-copolymer lithography and metal-assisted etching," *Adv. Funct. Mater.* **19**(15), 2495–2500 (2009).
- ²¹V. Schmidt, S. Senz, and U. Gösele, "Diameter-dependent growth direction of epitaxial silicon nanowires," *Nano Lett.* **5**(5), 931–935 (2005).
- ²²J. Huang, S. Y. Chiam, H. H. Tan, S. Wang, and W. K. Chim, "Fabrication of silicon nanowires with precise diameter control using metal nanodot arrays as a hard mask blocking material in chemical etching," *Chem. Mater.* **22**(13), 4111–4116 (2010).
- ²³Z. Huang, N. Geyer, P. Werner, J. de Boor, and U. Gösele, "Metal-assisted chemical etching of silicon: A review," *Adv. Mater.* **23**(2), 285–308 (2011).
- ²⁴T. Shimizu, T. Xie, J. Nishikawa, S. Shingubara, S. Senz, and U. Gösele, "Synthesis of vertical high-density epitaxial Si(100) nanowire arrays on a Si(100) substrate using an anodic aluminum oxide template," *Adv. Mater.* **19**(7), 917–920 (2007).
- ²⁵J. Svensson, P. Olausson, H. Menon, S. Lehmann, E. Lind, and M. Borg, "Three-dimensional integration of InAs nanowires by template-assisted selective epitaxy on tungsten," *Nano Lett.* **23**(11), 4756–4761 (2023).
- ²⁶R. Gupta, V. Chauhan, D. Gupta, S. Goel, and R. Kumar, in *Multifaceted Bio-Sensing Technology* (Elsevier, 2023), pp. 217–238.
- ²⁷Z. C. Meng, L. Y. Gao, and Z. Q. Liu, "Synthesis of Cu nanowires by template electrodeposition and their application in pressure sensors," *J. Electron. Mater.* **52**(5), 3463–3471 (2023).
- ²⁸F. Rostaie, S. Quednau, F. Weissenborn, and O. Birlem, "Low-resistance room-temperature interconnection technique for bonding fine pitch bumps," *J. Mater. Eng. Perform.* **30**(5), 3173–3177 (2021).
- ²⁹F. J. Wendisch, M. Rey, N. Vogel, and G. R. Bourret, "Large-scale synthesis of highly uniform silicon nanowire arrays using metal-assisted chemical etching," *Chem. Mater.* **32**(21), 9425–9434 (2020).
- ³⁰Y. Fu, A. Colli, A. Fasoli, J. Luo, A. Flewitt, A. Ferrari, and W. Milne, "Deep reactive ion etching as a tool for nanostructure fabrication," *J. Vac. Sci. Technol., B* **27**(3), 1520–1526 (2009).
- ³¹M. Rey, F. J. Wendisch, E. S. Aaron Goerlitzer, J. S. Julia Tang, R. S. Bader, G. R. Bourret, and N. Vogel, "Anisotropic silicon nanowire arrays fabricated by colloidal lithography," *Nanoscale Adv.* **3**(12), 3634–3642 (2021).
- ³²A. Mallavarapu, B. Gawlik, M. Grigas, M. Castañeda, O. Abed, M. P. C. Watts, and S. V. Sreenivasan, "Scalable fabrication and metrology of silicon nanowire arrays made by metal assisted chemical etch," *IEEE Trans. Nanotechnol.* **20**, 83–91 (2021).
- ³³S. Maurya, R. C. Muduli, and P. Kale, "Physical forces responsible for agglomeration of silicon nanowires arrays synthesized by metal-assisted chemical etching," *Russ. J. Phys. Chem. A* **97**(9), 1990–2000 (2023).
- ³⁴S. Gao, S. Hong, S. Park, H. Y. Jung, W. Liang, Y. Lee, C. W. Ahn, J. Y. Byun, J. Seo, M. G. Hahm, H. Kim, K. Kim, Y. Yi, H. Wang, M. Upmanyu, S. G. Lee, Y. Homma, H. Terrones, and Y. J. Jung, "Catalyst-free synthesis of sub-5 nm silicon nanowire arrays with massive lattice contraction and wide bandgap," *Nat. Commun.* **13**(1), 3467 (2022).
- ³⁵Z. Shi, K. Jefimovs, M. Stampanoni, and L. Romano, "High aspect ratio arrays of Si nano-pillars using displacement Talbot lithography and gas-MacEtch," *Mater. Sci. Semicond. Process.* **157**, 107311 (2023).
- ³⁶J. Parasuraman, A. Summanwar, F. Marty, P. Basset, D. E. Angelescu, and T. Bourouina, "Deep reactive ion etching of sub-micrometer trenches with ultra high aspect ratio," *Microelectron. Eng.* **113**, 35–39 (2014).
- ³⁷J. B. Sun and B. D. Almquist, "Interfacial contact is required for metal-assisted plasma etching of silicon," *Adv. Mater. Interfaces* **5**(24), 1800836 (2018).
- ³⁸S. Tachi, K. Tsujimoto, S. Arai, and T. Kure, "Low-temperature dry etching," *J. Vac. Sci. Technol., A* **9**(3), 796–803 (1991).
- ³⁹J. D. Kim, M. Kim, C. Chan, N. Draeger, J. J. Coleman, and X. Li, "CMOS-compatible catalyst for MacEtch: Titanium nitride-assisted chemical etching in vapor phase for high aspect ratio silicon nanostructures," *ACS Appl. Mater. Interfaces* **11**(30), 27371–27377 (2019).
- ⁴⁰L. L. Janavicius, J. A. Michaels, C. Chan, D. J. Sievers, and X. Li, "Programmable vapor-phase metal-assisted chemical etching for versatile high-aspect ratio silicon nanomanufacturing," *Appl. Phys. Rev.* **10**(1), 011409 (2023).
- ⁴¹F. Aydinoglu, A. Pan, C. Zhu, and B. Cui, "Effect of oxygen plasma cleaning on nonswitching pseudo-Bosch etching of high aspect ratio silicon pillars," *J. Vac. Sci. Technol., B* **38**(1), 012804 (2020).
- ⁴²B. Chang, P. Leussink, F. Jensen, J. Hübner, and H. Jansen, "DREM: Infinite etch selectivity and optimized scallop size distribution with conventional photoresists in an adapted multiplexed Bosch DRIE process," *Microelectron. Eng.* **191**, 77–83 (2018).
- ⁴³J. W. Coburn and H. F. Winters, "Conductance considerations in the reactive ion etching of high aspect ratio features," *Appl. Phys. Lett.* **55**(26), 2730–2732 (1989).
- ⁴⁴S. Tabara, "Effects of etching gases and bias frequency on notching and charging in high-density plasma," *Jpn. J. Appl. Phys.* **38**(6 A), 3753–3760 (1999).
- ⁴⁵I. W. Rangelow, "Critical tasks in high aspect ratio silicon dry etching for microelectromechanical systems," *J. Vac. Sci. Technol., A* **21**(4), 1550–1562 (2003).
- ⁴⁶Z. Ma, T. Guo, S. Cheng, Z. Song, J. Wang, and W. Yuan, "Fabrication of ultrahigh-aspect-ratio and periodic silicon nanopillar arrays using dislocation lithography and deep reactive-ion etching," *J. Micromech. Microeng.* **29**(10), 105011 (2019).
- ⁴⁷Y. J. Hung, S. L. Lee, B. J. Thibeault, and L. A. Coldren, "Fabrication of highly ordered silicon nanowire arrays with controllable sidewall profiles for achieving low-surface reflection," *IEEE J. Sel. Top. Quantum Electron.* **17**(4), 869–877 (2011).
- ⁴⁸M. M. Mirza, H. Zhou, P. Velha, X. Li, K. E. Docherty, A. Samarelli, G. Ternent, and D. J. Paul, "Nanofabrication of high aspect ratio ($\sim 50:1$) sub-10 nm silicon nanowires using inductively coupled plasma etching," *J. Vac. Sci. Technol., B* **30**(6), 06FF02 (2012).
- ⁴⁹K. O. Abrokwah, P. R. Chidambaram, and D. S. Boning, "Pattern based prediction for plasma etch," *IEEE Trans. Semicond. Manuf.* **20**(2), 77–86 (2007).
- ⁵⁰M. Huff, "Recent advances in reactive ion etching and applications of high-aspect-ratio microfabrication," *Micromachines* **12**(8), 991 (2021).
- ⁵¹M. J. De Boer, J. G. E. E. Gardeniers, H. V. Jansen, E. Smulders, M. J. Gilde, G. Roelofs, J. N. Sasserath, and M. Elwenspoek, "Guidelines for etching silicon MEMS structures using fluorine high-density plasmas at cryogenic temperatures," *J. Microelectromech. Syst.* **11**(4), 385–401 (2002).
- ⁵²J. Kiihamäki and S. Franssila, "Pattern shape effects and artefacts in deep silicon etching," *J. Vac. Sci. Technol., A* **17**(4), 2280–2285 (1999).
- ⁵³J. Karttunen, J. Kiihamäki, and S. Franssila, "Loading effects in deep silicon etching," *Proc. SPIE* **4174**, 90–97 (2000).

- ⁵⁴L. Sainiemi and S. Franssila, "Mask material effects in cryogenic deep reactive ion etching," *J. Vac. Sci. Technol.*, **B 25**(3), 801 (2007).
- ⁵⁵G. Hamdana, M. Descoins, T. Südkamp, D. Mangelinck, L. Caccamo, M. Bertke, H. S. Wasisto, H. Bracht, and E. Peiner, "Towards fabrication of 3D isotopically modulated vertical silicon nanowires in selective areas by nanosphere lithography," *Microelectron. Eng.* **179**, 74–82 (2017).
- ⁵⁶G. Hamdana, P. Puranto, Z. Li, F. Pohlenz, M. Xu, M. Bertke, H. S. Wasisto, U. Brand, and E. Peiner, "Nanoindentation of crystalline silicon pillars fabricated by soft UV nanoimprint lithography and cryogenic deep reactive ion etching," *Sens. Actuators, A* **283**, 65–78 (2018).
- ⁵⁷S. Tachi, K. Tsujimoto, and S. Okudaira, "Low-temperature reactive ion etching and microwave plasma etching of silicon," *Appl. Phys. Lett.* **52**(8), 616–618 (1988).
- ⁵⁸R. Dussart, T. Tillocher, P. Lefauchaux, and M. Boufnichel, "Plasma cryogenic etching of silicon: From the early days to today's advanced technologies," *J. Phys. D* **47**(12), 123001 (2014).
- ⁵⁹R. K. Dey, H. Ekinici, and B. Cui, "Effects of mask material conductivity on lateral undercut etching in silicon nano-pillar fabrication," *J. Vac. Sci. Technol.*, **B 38**(1), 012207 (2020).
- ⁶⁰C. A. Schneider, W. S. Rasband, and K. W. Eliceiri, "NIH image to ImageJ: 25 years of image analysis," *Nat. Methods* **9**(7), 671–675 (2012).
- ⁶¹E. Herth, S. Edmond, D. Bouville, J. L. Cercus, F. Bayle, and E. Cambri, "Micro-/nanopillars for micro- and nanotechnologies using inductively coupled plasmas," *Phys. Status Solidi A* **216**(23), 1900324 (2019).
- ⁶²J. Xu, A. Setiono, and E. Peiner, "Piezoresistive microcantilever with SAM-modified ZnO-nanorods@silicon-nanopillars for room-temperature parts-per-billion NO₂ detection," *ACS Appl Nano Mater.* **3**(7), 6609–6620 (2020).
- ⁶³M. Bertke, J. Xu, A. Setiono, I. Kirsch, E. Uhde, and E. Peiner, "Fabrication of a microcantilever-based aerosol detector with integrated electrostatic on-chip ultrafine particle separation and collection," *J. Micromech. Microeng.* **30**, 014001 (2020).
- ⁶⁴B. Gawlik, C. Barrera, E. T. Yu, and S. V. Sreenivasan, "Hyperspectral imaging for high-throughput, spatially resolved spectroscopic scatterometry of silicon nanopillar arrays," *Opt. Express* **28**(10), 14209 (2020).
- ⁶⁵B. Fodor, T. Defforge, E. Agócs, M. Fried, G. Gautier, and P. Petrik, "Spectroscopic ellipsometry of columnar porous Si thin films and Si nanowires," *Appl. Surf. Sci.* **421**, 397–404 (2017).
- ⁶⁶J. Grundmann, T. Käseberg, and B. Bodermann, "Characterisation of nanowire structures with scatterometric and ellipsometric measurements," *EPJ Web Conf.* **266**, 10003 (2022).
- ⁶⁷R. Sabbagh, A. Stothert, S. V. Sreenivasan, and D. Djurdjanovic, "Optical metrology of critical dimensions in large-area nanostructure arrays with complex patterns," *J. Manuf. Sci. Eng.* **145**(6), 061010 (2023).
- ⁶⁸M. Foldyna, A. S. Togonal, Rusli, and P. Roca i Cabarrocas, "Optimization and optical characterization of vertical nanowire arrays for core-shell structure solar cells," *Sol. Energy Mater. Sol. Cells* **159**, 640–648 (2017).
- ⁶⁹Z. Mrazkova, M. Foldyna, S. Misra, M. Al-Ghazaiat, K. Postava, J. Pištora, and P. Roca i Cabarrocas, "In-situ Mueller matrix ellipsometry of silicon nanowires grown by plasma-enhanced vapor-liquid-solid method for radial junction solar cells," *Appl. Surf. Sci.* **421**, 667–673 (2017).
- ⁷⁰M. Erfan, M. Gnambodoe-Capochichi, Y. Leprince-Wang, F. Marty, Y. M. Sabry, and T. Bourouina, "Nanowire length, density, and crystalline quality retrieved from a single optical spectrum," *Nano Lett.* **19**(4), 2509–2515 (2019).
- ⁷¹M. Erfan, L. M. Gnambodoe-Capochichi, F. Marty, Y. M. Sabry, T. Bourouina, and Y. Leprince-Wang, "Rapid assessment of nanomaterial homogeneity reveals crosswise structural gradients in zinc-oxide nanowire arrays," *Nanoscale* **12**(3), 1397–1405 (2020).
- ⁷²L. Siaudinyte, P. Hansen, R. Koops, J. Xu, and E. Peiner, "Hybrid metrology for nanometric energy harvesting devices," *Meas. Sci. Technol.* **34**, 094008 (2023).
- ⁷³S. Aachboun, P. Ranson, C. Hilbert, and M. Boufnichel, "Cryogenic etching of deep narrow trenches in silicon," *J. Vac. Sci. Technol.*, **A 18**(4), 2280–2285 (2000).
- ⁷⁴T. Zijlstra, E. van der Drift, M. J. A. de Dood, E. Snoeks, and A. Polman, "Fabrication of two-dimensional photonic crystal waveguides for 1.5 μm in silicon by deep anisotropic dry etching," *J. Vac. Sci. Technol.*, **B 17**(6), 2734 (1999).
- ⁷⁵M. J. Walker, "Comparison of Bosch and cryogenic processes for patterning high aspect ratio features in silicon," *Proc. SPIE* **4407**, 89–99 (2001).
- ⁷⁶Ü. Sökmen, A. Stranz, S. Fündling, S. Merzsch, R. Neumann, H. H. Wehmann, E. Peiner, and A. Waag, "Shallow and deep dry etching of silicon using ICP cryogenic reactive ion etching process," *Microsystem Technol.* **16**(5), 863–870 (2010).
- ⁷⁷B. Wu, A. Kumar, and S. Pamarthy, "High aspect ratio silicon etch: A review," *J. Appl. Phys.* **108**(5), 051101 (2010).
- ⁷⁸F. Laermer, S. Franssila, L. Sainiemi, and K. Kolari, *Deep Reactive Ion Etching* (Elsevier Inc., 2015).
- ⁷⁹J. R. Ligenza, "Effect of crystal orientation on oxidation rates of silicon in high pressure steam," *J. Phys. Chem.* **65**(11), 2011–2014 (1961).
- ⁸⁰F. R. McFEELY, J. F. MORAR, and F. J. GIMPSEL, "Soft X-ray photoemission study of the silicon-fluorine etching reaction," *Surf. Sci.* **165**, 277–287 (1986).
- ⁸¹J. K. Prüßing, T. Böckendorf, F. Kipke, J. Xu, P. Puranto, J. Lundsgaard Hansen, D. Bougeard, E. Peiner, and H. Bracht, "Retarded boron and phosphorus diffusion in silicon nanopillars due to stress induced vacancy injection," *J. Appl. Phys.* **131**, 075702 (2022).
- ⁸²Y. H. Lee, M. Chen, Y. H. Lee, Y. H. Lee, and M. Chen, "Silicon doping effects in reactive plasma etching," *J. Vac. Sci. Technol.*, **B 4**(2), 468 (1986).
- ⁸³S. Merzsch, F. Steib, H. S. Wasisto, A. Stranz, P. Hinze, T. Weimann, E. Peiner, and A. Waag, "Production of vertical nanowire resonators by cryogenic-ICP-DRIE," *Microsystem Technol.* **20**(4–5), 759–767 (2014).
- ⁸⁴J. Xu, M. Bertke, X. Li, H. Mu, H. Zhou, F. Yu, G. Hamdana, A. Schmidt, H. Bremers, and E. Peiner, "Fabrication of ZnO nanorods and Chitosan@ZnO nanorods on MEMS piezoresistive self-actuating silicon microcantilever for humidity sensing," *Sens. Actuators, B* **273**, 276–287 (2018).
- ⁸⁵G. S. Oehrlein, J. F. Rembetski, and E. H. Payne, "Study of Sidewall Passivation and Microscopic Silicon Roughness Phenomena in Chlorine-Based," *J. Vac. Sci. Technol.*, **B 8**, 1199 (1990).
- ⁸⁶H. V. Jansen, M. J. De Boer, S. Unnikrishnan, M. C. Louwerse, and M. C. Elwenspoek, "Black silicon method X: A review on high speed and selective plasma etching of silicon with profile control: An in-depth comparison between Bosch and cryostat DRIE processes as a roadmap to next generation equipment," *J. Micromech. Microeng.* **19**(3), 033001 (2009).
- ⁸⁷R. F. Pease and S. Chou, "Lithography and other patterning techniques for future electronics," *Proc. IEEE* **96**(2), 248–270 (2008).
- ⁸⁸R. P. Seisyan, "Nanolithography in microelectronics: A review," *Tech. Phys.* **56**(8), 1061–1073 (2011).
- ⁸⁹A. Pimpin and W. Srituravanich, "Reviews on micro- and nanolithography techniques and their applications," *Eng. J.* **16**(1), 37–55 (2012).
- ⁹⁰Y. Chen, "Nanofabrication by electron beam lithography and its applications: A review," *Microelectron. Eng.* **135**, 57–72 (2015).
- ⁹¹M. Hatzakis, "Electron resists for microcircuit and mask production," *J. Electrochem. Soc.* **116**(7), 1033 (1969).
- ⁹²X. Xu, Q. Yang, N. Wattanatorn, C. Zhao, N. Chiang, S. J. Jonas, and P. S. Weiss, "Multiple-patterning nanosphere lithography for fabricating periodic three-dimensional hierarchical nanostructures," *ACS Nano* **11**(10), 10384–10391 (2017).
- ⁹³I. Park, H.-J. Han, Y. S. Jung, M. Cho, and M. Gao, "Hydrogen sensors: Palladium-decorated silicon nanomesh fabricated by nanosphere lithography for high performance, room temperature hydrogen sensing," *Small* **14**(10), 1703691 (2018).
- ⁹⁴L. Li, Y. Fang, C. Xu, Y. Zhao, K. Wu, C. Limburg, P. Jiang, and K. J. Ziegler, "Controlling the geometries of Si nanowires through tunable nanosphere lithography," *ACS Appl. Mater. Interfaces* **9**(8), 7368–7375 (2017).
- ⁹⁵D. Ji, T. Li, and H. Fuchs, "Nanosphere lithography for sub-10-nm nanogap electrodes," *Adv. Electron. Mater.* **3**(1), 1600348 (2017).
- ⁹⁶S. Su, L. Lin, Z. Li, J. Feng, and Z. Zhang, "The fabrication of large-scale sub-10-nm core-shell silicon nanowire arrays," *Nanoscale Res. Lett.* **8**(1), 405 (2013).
- ⁹⁷W. M. Choi and O. O. Park, "A soft-imprint technique for direct fabrication of submicron scale patterns using a surface-modified PDMS mold," *Microelectron. Eng.* **70**(1), 131–136 (2003).
- ⁹⁸M. Bender, U. Plachetka, J. Ran, A. Fuchs, B. Vratzov, H. Kurz, T. Glinsner, and F. Lindner, "High resolution lithography with PDMS molds," *J. Vac. Sci. Technol.*, **B 22**(6), 3229 (2004).

- ⁹⁹U. Plachetka, M. Bender, A. Fuchs, B. Vratzov, T. Glinsner, F. Lindner, and H. Kurz, "Wafer scale patterning by soft UV-nanoimprint lithography," *Microelectron. Eng.* **73–74**, 167–171 (2004).
- ¹⁰⁰N. Koo, M. Bender, U. Plachetka, A. Fuchs, T. Wahlbrink, J. Bolten, and H. Kurz, "Improved mold fabrication for the definition of high quality nanopatterns by soft UV-nanoimprint lithography using diluted PDMS material," *Microelectron. Eng.* **84(5–8)**, 904–908 (2007).
- ¹⁰¹A. Cattoni, E. Cambil, D. Decanini, G. Faini, and A. M. Haghiri-Gosnet, "Soft UV-NIL at 20 nm scale using flexible bi-layer stamp casted on HSQ master mold," *Microelectron. Eng.* **87(5–8)**, 1015–1018 (2010).
- ¹⁰²M. Leitgeb, D. Nees, S. Ruttloff, U. Palfinger, J. Götz, R. Liska, M. R. Belegatis, and B. Stadlober, "Multilength scale patterning of functional layers by roll-to-roll ultraviolet-light-assisted nanoimprint lithography," *ACS Nano* **10(5)**, 4926–4941 (2016).
- ¹⁰³G. Hamdana, "MEMS piezoresistive force sensors based on micro-/nanostructured silicon components," Dissertation, Technische Universität Braunschweig, 2019.
- ¹⁰⁴L. Crouzier, A. Delvallée, S. Ducourtieux, L. Devoille, G. Noircler, C. Ulysse, O. Taché, E. Barruet, C. Tromas, and N. Feltin, "Development of a new hybrid approach combining AFM and SEM for the nanoparticle dimensional metrology," *Beilstein J. Nanotechnol.* **10**, 1523–1536 (2019).
- ¹⁰⁵M. Foldyna, A. De Martino, D. Cattelan, F. Bogeat, C. Licitra, J. Foucher, P. Barritault, and J. Hazart, "Accurate dimensional characterization of periodic structures by spectroscopic Mueller polarimetry," *Proc. SPIE* **7140**, 71400I (2008).
- ¹⁰⁶S. Ben Hatit, M. Foldyna, A. De Martino, and B. Drévilion, "Angle-resolved Mueller polarimeter using a microscope objective," *Phys. Status Solidi A* **205(4)**, 743–747 (2008).
- ¹⁰⁷S.-Y. Lu and R. A. Chipman, "Interpretation of Mueller matrices based on polar decomposition," *J. Opt. Soc. Am. A* **13(5)**, 1106–1113 (1996).
- ¹⁰⁸P. E. Hansen, S. R. Johannsen, S. A. Jensen, and J. S. M. Madsen, "Enhanced measurement accuracy for nanostructures using hybrid metrology," *Front. Phys.* **9**(January), 791459 (2022).
- ¹⁰⁹M. H. Madsen and P. E. Hansen, "Scatterometry-fast and robust measurements of nano-textured surfaces," *Surf. Topogr.* **4(2)**, 023003 (2016).
- ¹¹⁰S. Ducourtieux and B. Poyet, "Development of a metrological atomic force microscope with minimized Abbe error and differential interferometer-based real-time position control," *Meas. Sci. Technol.* **22(9)**, 094010 (2011).
- ¹¹¹A. Alipour, K. T. Arat, H. Alemansour, L. Montes, J. Gardiner, J. Diederichs, B. Colvin, A. Amann, K. Jensen, W. Neils, S. Spagna, L. Stühn, S. Seibert, H. Frerichs, M. Wolff, and C. H. Schwalb, "A highly integrated AFM-SEM correlative analysis platform," *Microsc. Today* **31(6)**, 17–22 (2023).